

NASA ERA Integrated CFD for Wind Tunnel Testing of Hybrid Wing-Body Configuration

Joseph A. Garcia¹, John E. Melton², Michael Schuh², Kevin D. James³, Kurtis R. Long⁴
NASA Ames Research Center, Moffett Field, CA, 94035, USA

Dan D. Vicroy⁵, Karen A. Deere⁶, James M. Luckring⁷, Melissa B. Carter⁴, Jeffrey D. Flamm⁵
NASA Langley Research Center, Hampton VA, 23681, USA

Paul M. Stremel⁸, Ben E. Nikaido⁹, Robert E. Childs¹⁰
Science and Technology Corporation, NASA Research Park, CA, 94035, USA

The NASA Environmentally Responsible Aviation (ERA) Project explored enabling technologies to reduce impact of aviation on the environment. One project research challenge area was the study of advanced airframe and engine integration concepts to reduce community noise and fuel burn. To address this challenge, complex wind tunnel experiments at both the NASA Langley Research Center's (LaRC) 14'x22' and the Ames Research Center's 40'x80' low-speed wind tunnel facilities were conducted on a BOEING Hybrid Wing Body (HWB) configuration. These wind tunnel tests entailed various entries to evaluate the propulsion-airframe interference effects, including aerodynamic performance and aeroacoustics. In order to assist these tests in producing high quality data with minimal hardware interference, extensive Computational Fluid Dynamic (CFD) simulations were performed for everything from sting design and placement for both the wing body and powered ejector nacelle systems to the placement of aeroacoustic arrays to minimize its impact on vehicle aerodynamics. This paper presents a high-level summary of the CFD simulations that NASA performed in support of the model integration hardware design as well as the development of some CFD simulation guidelines based on post-test aerodynamic data. In addition, the paper includes details on how multiple CFD codes (OVERFLOW, STAR-CCM+, USM3D, and FUN3D) were efficiently used to provide timely insight into the wind tunnel experimental setup and execution.

Nomenclature

A	=	Effective projected vehicle area
C _D	=	Drag coefficient
C _L	=	Lift coefficient
C _m	=	Pitching moment coefficient
C _{mα}	=	Pitching moment coefficient curve slope variation with angle of attack, /deg.
C _T	=	Thrust coefficient
L _B	=	Body Length

¹ Aerospace Engineer, System Analysis Office, Aeronautics Directorate, Mail Stop 258-1, AIAA Senior Member.

² Aerospace Engineer, System Analysis Office, Aeronautics Directorate, Mail Stop 258-1.

³ Aerospace Engineer, Experimental Aero-Physics Branch, Mail Stop 260-1, AIAA Associate Fellow.

⁴ Aerospace Engineer, Experimental Aero-Physics Branch, Mail Stop 260-1.

⁵ Senior Researcher, Flight Dynamics Branch, Research Directorate, MS 308, AIAA Associate Fellow.

⁶ Aerospace Engineer, Configuration Aerodynamics Branch, Mail Stop 499, AIAA Senior Member.

⁷ Aerospace Engineer, Configuration Aerodynamics Branch, Mail Stop 499, AIAA Associate Fellow.

⁸ Senior Research Scientist, Science and Technology Corporation, Mail Stop 258-1, AIAA Member.

⁹ Research Scientist, Science and Technology Corporation, Mail Stop 258-1, AIAA Member.

¹⁰ Senior Research Scientist, Science and Technology Corporation, Mail Stop 258-1.

L_{B_REF}	=	Reference Body Length
L/D	=	Lift-to-drag ratio
Re	=	Reynolds Number
R_{cref}	=	Reynolds number based on c_{ref} , U_{cref} / ν
S_{wet}	=	Wetted vehicle surface area
St	=	Strouhal number
U	=	free stream reference velocity
M_∞	=	Free-stream Mach number
α	=	angle of attack, deg.
μ	=	viscosity
ν	=	kinematic viscosity, μ/ρ
ρ	=	density
ρ_∞	=	Free-stream density

Acronyms

ARC	Ames Research Center
CFD	Computational Fluid Dynamics
CAD	Computer Aided Design
ERA	Environmentally Responsible Aviation
EPNdB	Effective Perceived Noise level in decibels
FTN	Flow Through Nacelle
HWB	Hybrid Wing Body
LaRC	Langley Research Center
LM	Langtry-Menter transitional turbulence model
NASA	National Aeronautics and Space Administration
PAI	Propulsion Airframe Integration
SA	Spalart-Allmaras turbulence model
SST	Shear Stress Transport turbulence model
TPS	Turbine Propulsion Simulator

I. Introduction

Achieving ultra-efficient commercial vehicles is one of NASA's Aeronautics Research Mission Directorate's technology goals. The Environmentally Responsible Aviation (ERA) project was formed to help achieve this goal by exploring ways to reduce the impact of aviation on the environment specifically in the areas of noise, emissions and fuel burn^{1,2}. To this end, a campaign of wind tunnel experiments was performed on a 5.75% scale model of the BOEING Hybrid Wing Body (HWB) configuration 0009GM (Fig. 1) for evaluation of engine/airframe operability in the following four model configurations: Flow Through Nacelle (FTN), Ejector, Turbine Propulsion Simulators (TPS), and Aeroacoustics.

NASA's experience with modern wind tunnel testing has shown that utilizing Computational Fluid Dynamics (CFD) to help guide and answer questions before, during, and after a test has been a valuable endeavor. This experience has most recently been demonstrated in NASA's Orion program with its successful Pad Abort-1 and Exploration Flight Test-1. Within the Orion program, an Aerosciences project consisting of both simulation and experimental experts worked in conjunction toward a complimentary set of wind tunnel tests and CFD simulations that contributed to the success of these two flight tests. The recent HWB test campaign was a similarly successful cross-center, cross-discipline, and cross-partner collaboration.

II. Efficient use of Multiple CFD solvers

The following section includes details on the different CFD solvers and explains how each tool was used to provide insight into the ERA wind tunnel experiments; specifically in the area of predicting aerodynamic interference due to model support structures, as well as assessing alternate support options that reduced unwanted effects.

NASA's access to high-end computing (HEC) and modern CFD solvers has enabled the use of computational simulations in the development, design and testing of a variety of aerospace vehicle studies. While there are some limitations on how quickly these CFD simulations can be generated, due to preparation time required for CFD-ready CAD/geometry, the substantial HEC resources available within NASA has made it possible to utilize higher-fidelity CFD simulations to provide insight into the complex aerodynamic flows studied in the HWB wind tunnel campaign.

Our experience has shown that the use of multiple CFD tools with both varying and duplicative fidelity provides a basis for CFD uncertainties and is a valuable approach to identifying CFD implementation errors. Furthermore, each CFD tool has its own strengths that enable addressing various questions ranging from preliminary assessments to final flight vehicle aerodynamic database creation. For example, when a wind tunnel test is being formulated for internal flow problems, an unstructured viscous CFD solver tools such as the commercial tool STAR-CCM+³, which has a very robust CAD-to-mesh capability, has been invaluable in quickly generating the complex mesh geometries and predicting the associated flow solutions. In the case of generating large flight databases, such as the aerodynamic databases required for the guidance, navigation, and controls assessment for NASA's Orion vehicle, the use of CFD tools such as NASA's OVERFLOW⁴ and FUN3D⁵ solvers becomes increasingly valuable as they provide higher-order methods that are easily scalable on supercomputers. Hundreds of OVERFLOW and FUN3D simulations can also be generated simultaneously due to freedom from licensing restrictions.

A. Geometry and Mesh Generation

Properly modeling the geometry in a CFD simulation is an absolute necessity, especially in regions of attached flow. Therefore, the fidelity of the CFD geometry must be as precise as possible. This requires the CFD to be based on accurate CAD definitions of the vehicle of interest, including all model support structure in the case of a wind tunnel experiment. However, there are sometimes benefits to considering geometry simplification in regions where the flow is separated, such as around support structures that may not affect the vehicle aerodynamics but can introduce overly complex geometry and unsteadiness in the flow requiring expensive time-resolved simulations. This balance of geometry fidelity versus simplification requires experience and careful assessment of the effects at select flow conditions for the problem at hand.

At times, it is beneficial to model all the complex details of the geometry including support structures, especially with CFD tools that lend themselves to this approach, such as unstructured CFD solvers that simplify mesh generation. The commercial CFD solver, STAR-CCM+³, is one such tool that was heavily utilized in the process of answering key question raised by the experimentalists for the various wind tunnel entries.

Figures 2 through 5 show examples of the typical meshes generated for each of the four CFD solvers used. The OVERFLOW flow solver utilized a system of overset structured grids (Fig. 2) developed with the chimera grid tools (CGT)⁶ version 2.1q and overset grid connectivity generated by Pegasus version 5.2⁷. The y^+ boundary layer normal grid spacing at the wall was approximately 1.0 or less. The STAR-CCM+ flow solver utilized polyhedral meshes (Fig. 3) that were directly generated from CAD with a y^+ boundary layer normal grid spacing value equal to approximately 1.0 or less for the first prism layer off the no-slip wall boundaries. The USM3D flow solver utilized a system of tetrahedral, cell-centered, finite volume unstructured meshes (Fig. 4) created by the TetrUSS GridTool⁸ software and the volume mesh generation software, VGRID/POSTGRID^{9,10}, which maintained a y^+ boundary layer wall normal grid spacing value of approximately 0.5 or less. The FUN3D flow solver utilized a system of unstructured grids based partially on the same surface mesh as those used in STAR-CCM+. When surface geometry modifications to the baseline meshes were needed, the commercial Pointwise¹¹ mesh generation software version 17.3R1 was used. All unstructured volume meshes for FUN3D were generated using the Advancing-Front Local-Reconnection (AFLR3)¹² software and maintained a boundary layer y^+ normal wall spacing value equal to approximately 1.0 or less.



Figure 1. HWB model cruise configuration in NASA LaRC 14'x22' wind tunnel.

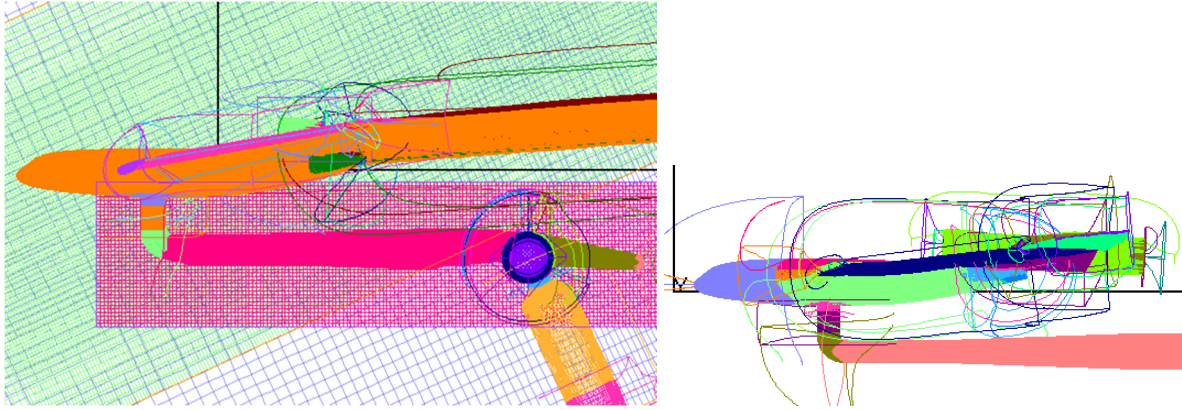


Figure 2. Overset grids of the HWB in the LaRC 14'x22' wind tunnel facility.

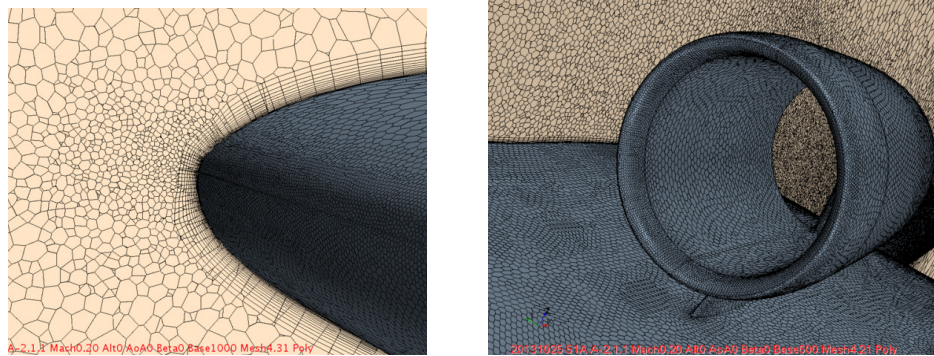


Figure 3. STAR-CCM+ Unstructured polyhedral mesh of the HWB.

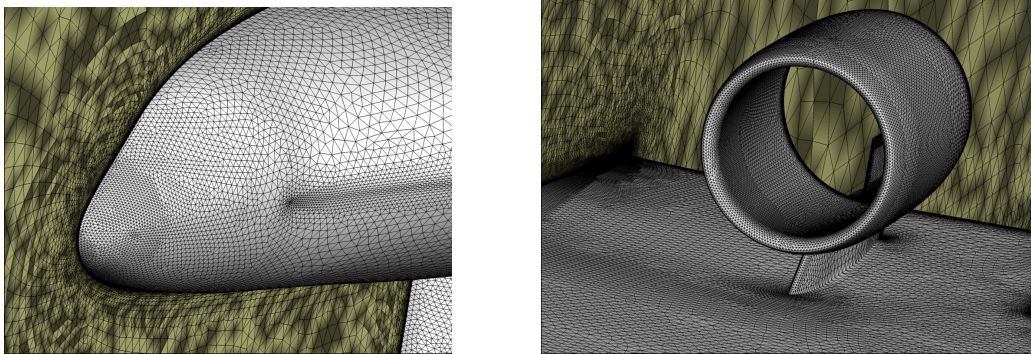


Figure 4. Unstructured USM3D mesh of the HWB.

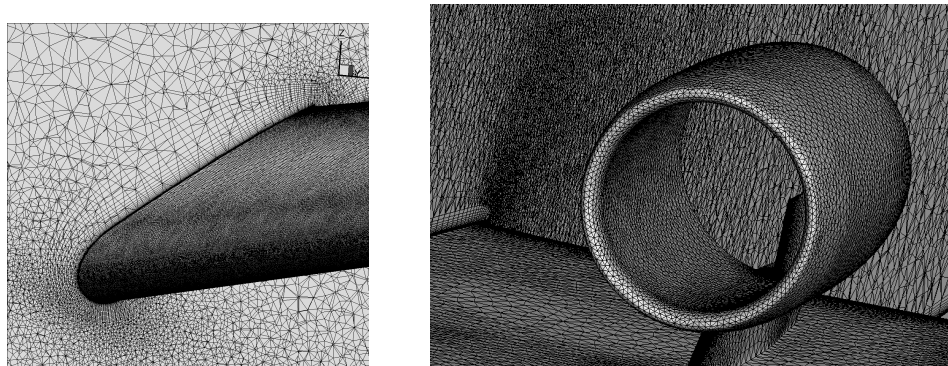


Figure 5. Unstructured FUN3D mesh of the HWB.

B. Turbulence Modeling

All of the CFD solvers used during this study were run using the Reynolds-Averaged Navier-Stokes modeling option and an associated turbulence model. The turbulence modeling had a significant effect on the predicted aerodynamics of the HWB, especially as the onset of turbulent boundary layer separation affected the maximum lift at high angles of attack. Several turbulence modeling options were explored amongst the various CFD solvers, including the Spalart-Allmaras¹³ (SA), Menter's SST¹⁴, and Langtry-Menter¹⁵ models. The Langtry-Menter model was only used to provide a laminar-turbulent transition capability to assess tripping strategies (summarized in the "Trip dot placement selection" section below).

In addition, simulations of high-lift configurations on conventional wings often benefit from various forms of "rotation and curvature" (RC) corrections to the turbulence models¹⁶. The SA-RC model¹⁷ was evaluated in some simulations, and the RC option was also explored within the SST model for some initial simulations. The Quadratic Constitutive Relation (QCR) model^{18,19} was also considered.

While multiple turbulent modeling options were assessed, the majority of results were produced assuming "fully turbulent" flow using the native implementation of the favored turbulence model in each CFD solver for these flows. The majority of predictions done with OVERFLOW used the SA model. For STAR-CCM+, the SST model was preferred. For FUN3D and USM3D, the SA model was principally used.

C. CFD Solver Options

Simulations generated by CD-adapco's STAR-CCM+ were run by NASA Ames Research Center using the Reynolds-Averaged Navier-Stokes, K-Omega SST (Menter) turbulence model based on Version 9.04.009 of the code with the segregated solver and Roe flux, 2nd order scheme.

Simulations generated by OVERFLOW, developed and distributed by NASA Langley Research Center, were generated by NASA Ames Research Center with spatial discretization of the Euler terms using the third-order HLLC upwind scheme. The time integration employed depended upon the nature of the solution. For most of the lower angle of attack simulations, runs were started with the "steady-state mode" of integration and simple time-stepping. Simulations that converged to a steady-state flow solution using this option were considered complete. At higher angles of attack, many flows exhibited asymptotic unsteadiness, and these were solved using the "time-accurate mode," with subiterations inside the outer second-order backward-difference time integration algorithm. Viscous fluxes were computed with second-order central spatial discretization. Solutions were computed with both the SA and SST models, which were solved with the same discretization accuracy as the mean flow variables.

Simulations generated by USM3D²⁰, developed by NASA Langley Research Center as part of the NASA Tetrahedral Unstructured Software System²¹ (TetrUSS), were run by NASA LaRC with the implicit Gauss-Seidel scheme and the Roe flux-difference splitting scheme. The code was run with first-order spatial accuracy until the residual dropped two orders of magnitude. USM3D then automatically switched to generate second-order spatially accurate solutions until full convergence. The SA turbulence model was used for all of the flow conditions.

Simulations generated by FUN3D⁵, developed and distributed by NASA Langley Research Center, were run by NASA Ames Research Center utilizing version 12.7 with a node-based, finite-volume spatial discretization. The Roe flux-splitting scheme was used for the Euler terms. The time integration employed depended on the nature of the solution. For most of the lower angle of attack simulations, solutions were generated using the "steady-state mode" of integration, with a point-implicit simple time-stepping method. In "steady-state mode," FUN3D was initially run with first-order spatial accuracy until the residual dropped three orders of magnitude, at which point the spatial accuracy was increased to second-order. At higher angles of attack, many flows exhibited asymptotic unsteadiness, and these were solved using the "time-accurate mode," with subiterations inside the outer time integration algorithm. All solutions were computed with the SA turbulence model.

D. CFD Simulation Quality Assessment

When using CFD to assess a large matrix of flow conditions and/or configurations, the management, post-processing, and quality assessment of the numerous and large data sets can become burdensome. To alleviate this load in the current work, we leveraged tools developed under the NASA Orion Aerosciences and previous ARMD projects. Some such tools included automated convergence scripts that were used to monitor and control unsteady flow simulations and an HTML-based visualization software referred to as the 'miniwall'. Utilizing the miniwall, we were able to automate the visualization of a variety of results from convergence plots to surface pressure contours in a logical matrix format. A depiction of the miniwall tool and one of its screens is shown in Fig. 6. The generation of the CFD images of interest can be obtained using the plotting software of choice, but careful scripting of this process is necessary to generate the required file tree structure that enables the miniwall to automatically populate its matrix array of windows. Essentially, it mimics a wall of video monitors similar to what the NASA HEC facility refers to as

the ‘hyperwall’²². Through this process, we were able to manage the various CFD simulations being run, perform quality assessments, and more efficiently provide feedback to the project on various requested CFD wind tunnel support tasks.

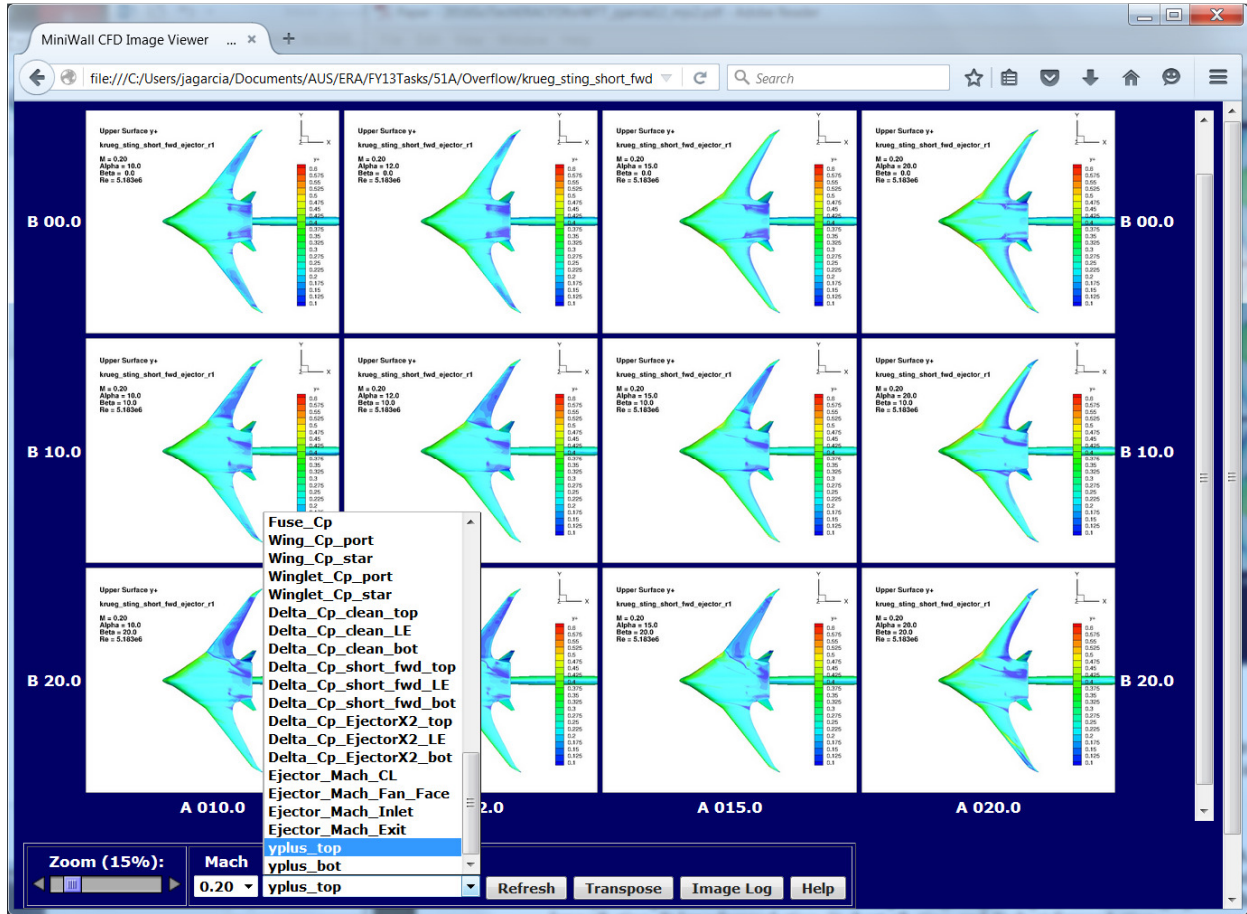


Figure 6. Sample miniwall application.

III. CFD Wind Tunnel Support

The use of CFD to guide the design and selection of the various wind tunnel support structures and assess their interference effects on the overall vehicle aerodynamics (including producing aerodynamic increments to be used to adjust wind tunnel data) is highlighted in the following section.

A. Sting Configuration and Placement

To help determine the proper sting configuration for the HWB model, the NASA CFD group evaluated four sting configurations to guide the down selection to one that minimized its aerodynamic influence on the HWB during testing. These were all simulated in free-air to remove the complexity of modeling the walls. Fig. 7 depicts the four sting options the project considered: 1) long aft sting, 2) long forward sting, 3) short aft sting, and 4) short forward sting. Where ‘forward’ and ‘aft’ refers to the sting attachment distance relative to the nose of the vehicle; the ‘short’ and ‘long’ refers to the distance of the sting elbow below the vehicle.

The four sting configurations were initially simulated with OVERFLOW and the integrated coefficients for lift (C_L), drag (C_D) and side (C_S) force along with roll moment (C_l), pitch moment (C_m) and yaw moment (C_n) are shown in Figs. 8 and 9. A baseline configuration without a sting, referred to as ‘clean’, was used to provide the basis to assess the sting increments. The HWB geometry configuration that was analyzed in these simulation was based on the Boeing HWB 0009D cruise wing configuration in free air (no wind tunnel walls). For the zero sideslip results in Fig. 8, the largest force and moment increment from the baseline ‘clean’ configuration are seen in the ‘long aft’ and ‘short aft’ sting configurations (specifically in the drag, lift, and pitch moment coefficients). Similar increment trends are seen in the results for the 20 degrees sideslip cases shown in Fig. 9.

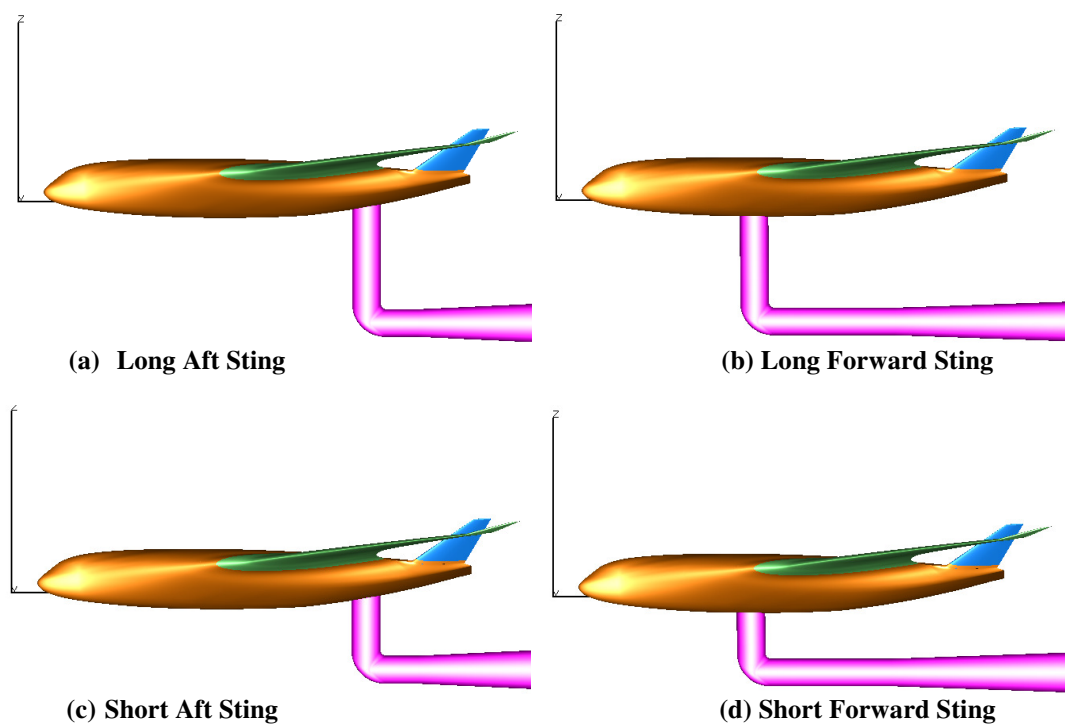


Figure 7. Wind tunnel sting configurations considered.

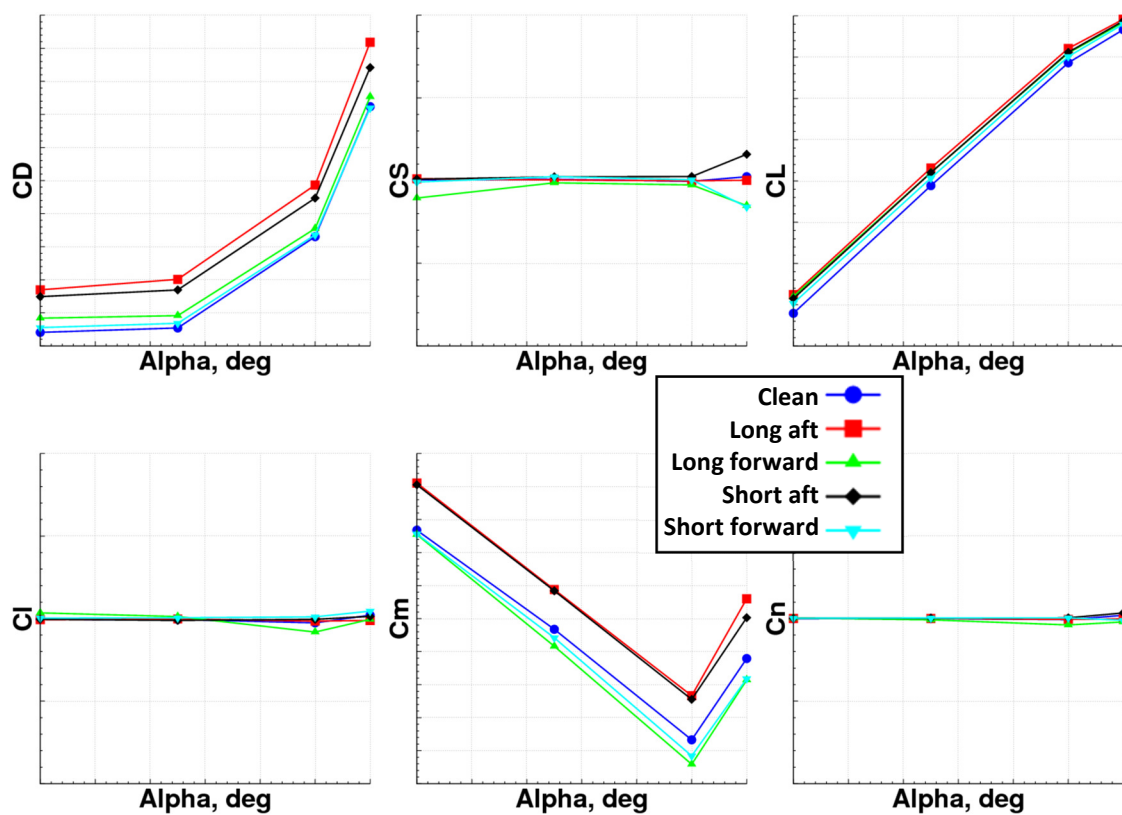


Figure 8. OVERFLOW sting configuration force and moment comparison for 0 degree sideslip.

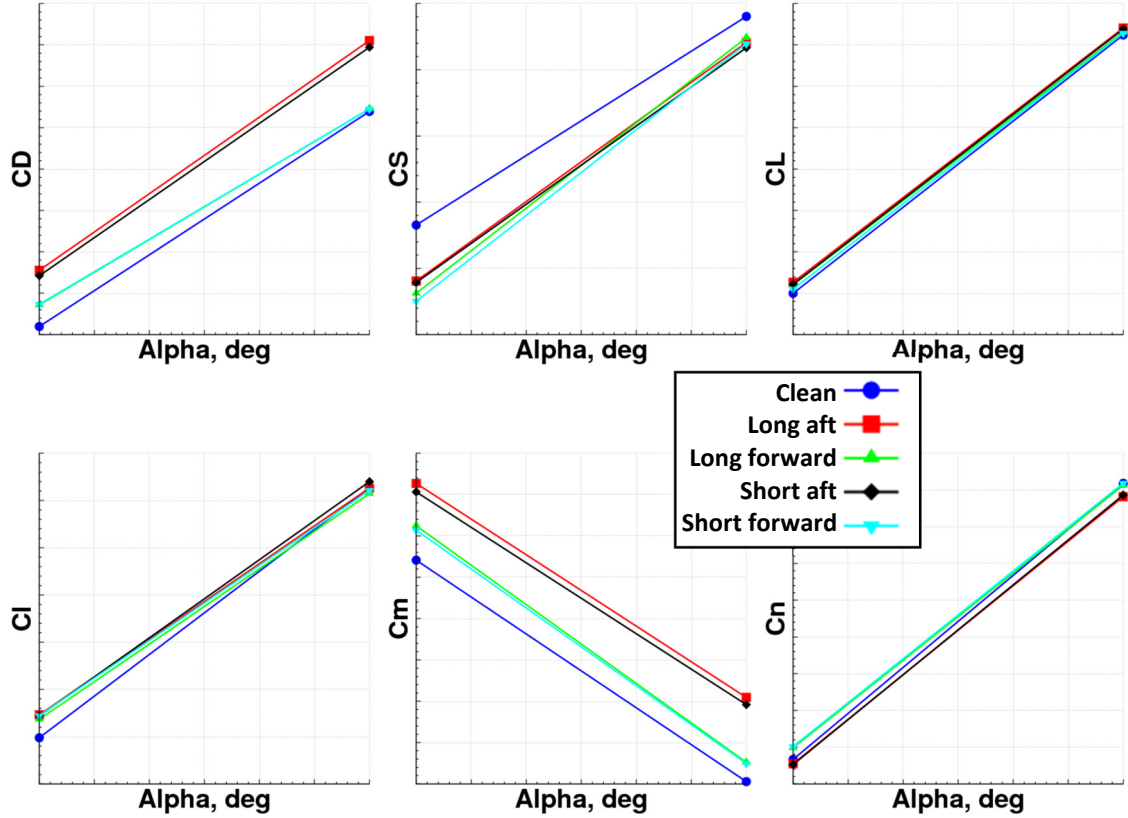


Figure 9. OVERFLOW sting configuration force and moment comparison for 20 degree sideslip.

The predicted integrated forces and moments indicated that the long forward and short forward stings exhibited the least influence on the overall vehicle load. However, it was still not clear which of the two forward stings to choose from as they both had nearly identical increments. In order to further investigate this, plots of delta surface pressure coefficient ($\Delta C_p = C_{p_support} - C_{p_clean}$) contour were generated to show the differences in C_p between a given sting configuration and the clean configuration for both the long forward and short forward sting at an angle of attack of 12 degree with 0 and 20 degrees side slip. The lower surface delta C_p contours are shown in Fig. 10 and the upper surface contours are shown in Fig. 11. This delta C_p approach provided a good way to visualize the local flow on the surface due to the influence of features such as the given sting configuration. The contour levels are plotted to show positive pressure delta in red and negative pressure delta in blue. The goal is to achieve zero delta values, shown as nearly white contours in the plots, indicating minimal interference due to the presence of a given sting configuration. Most of the vehicle lower surface has near-zero delta C_p 's, except around the location where the sting is present. Fig. 11 shows larger visual deltas appearing on the upper surface of the wing near the wing crank, with the largest deltas coming from the 'Long Forward' sting.

Additional CFD simulations were generated using the USM3D solver to provide a secondary check on the OVERFLOW results. Figure 12 shows the USM3D-predicted delta C_p distribution on the lower surface for all four stings options at an angle of attack of 10 degrees with 0 degrees sideslip. The largest difference is the increased pressure upstream of the aft sting configurations which spreads out onto the wing. This increased pressure on the lower side of the wing is consistent with the higher lift predicted by OVERFLOW as shown in the load coefficient plots of Fig. 8. Comparison of the long and short forward stings showed that the blockage of the long forward sting strongly influenced the flow on the upper wing surface. In addition, the wake generated by the long forward sting is larger, as indicated by the Mach contours along the symmetry plane of Fig. 13.

Based on these CFD findings, the recommendation was to use the short forward sting configuration for all the testing in both the 14'x22' and 40'x80' wind tunnels.

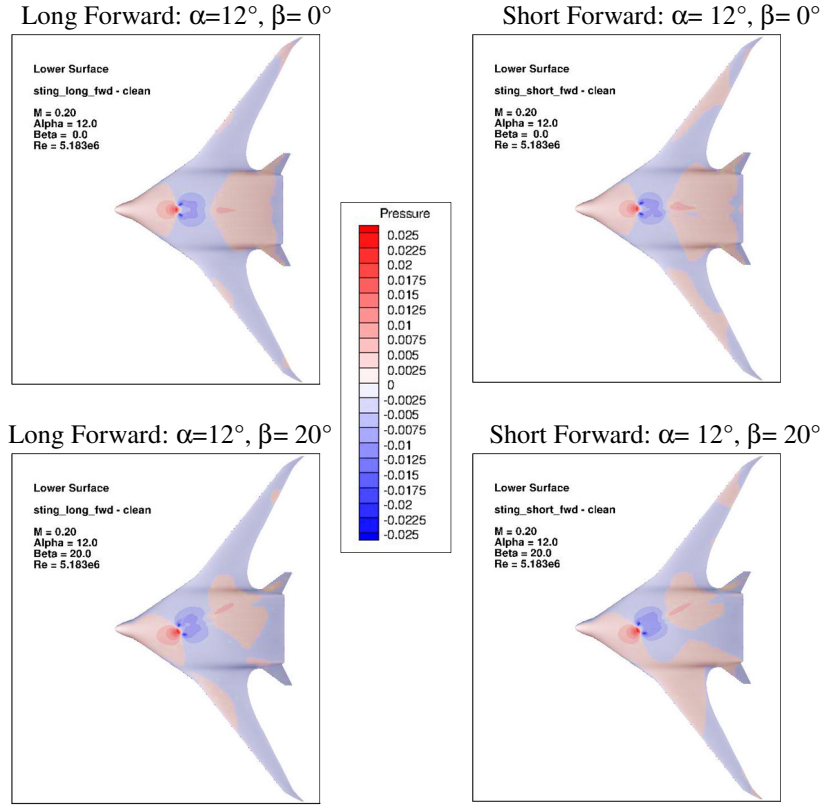


Figure 10. OVERFLOW long vs. short forward sting lower surface ΔC_p =(Sting– Clean).

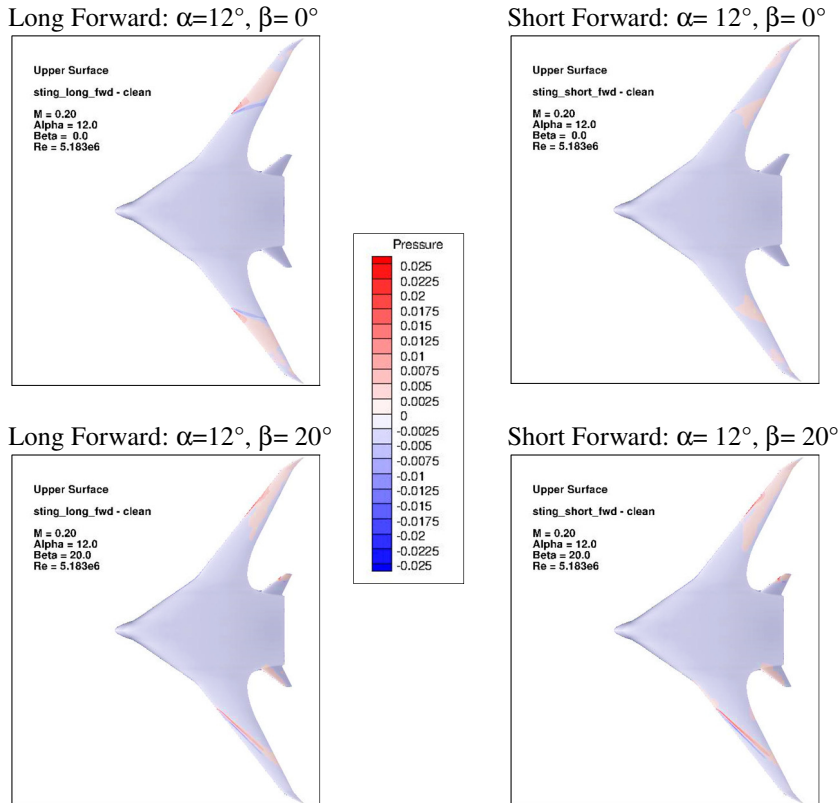


Figure 11. OVERFLOW long vs. short forward sting upper surface ΔC_p =(Sting– Clean).

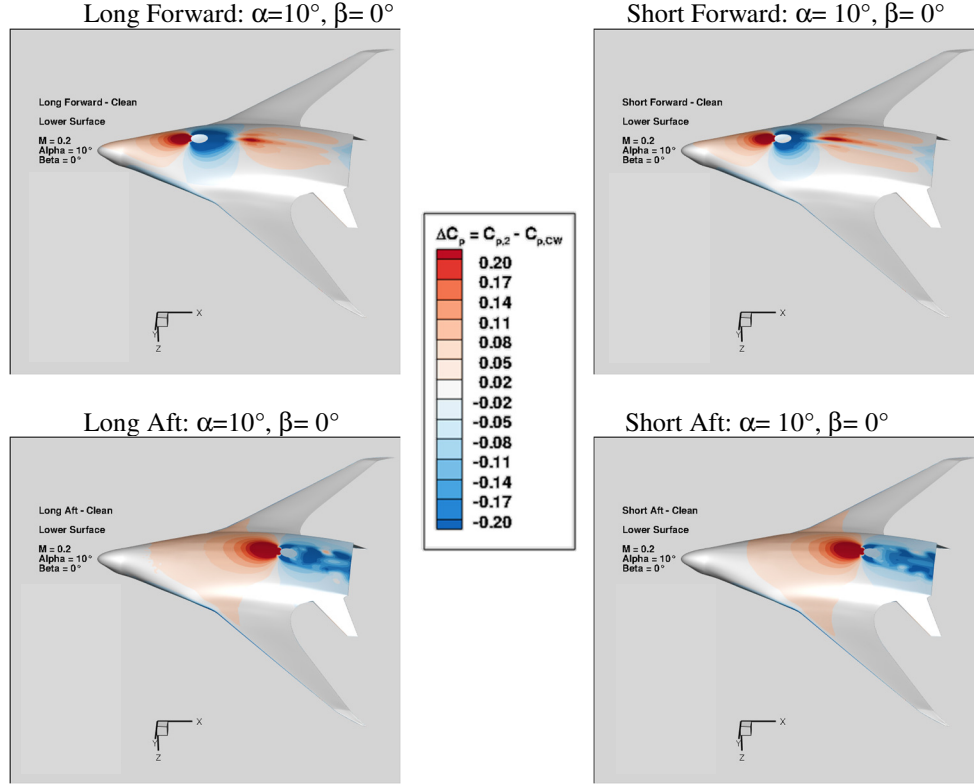


Figure 12. USM3D sting effects on lower surface ΔC_p =(Sting- Clean).

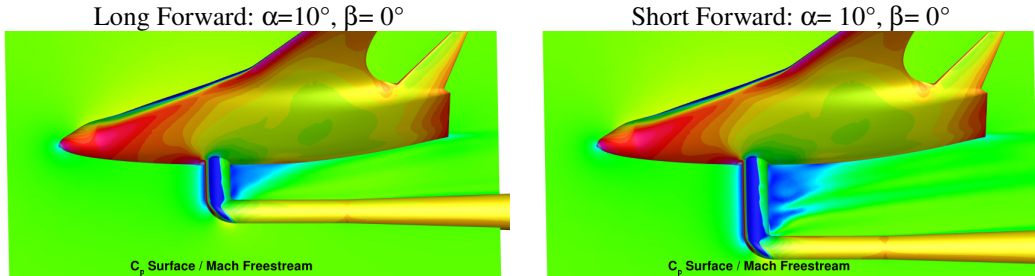


Figure 13. USM3D long vs. short forward sting wake comparisons.

B. Ejector Selection

The NASA CFD group also evaluated two ejector configurations, which were designed to produce flow distortion over the wing equivalent to that expected on a full scale flight vehicle. The two ejector options included a baseline ejector (referred to as 'eject_r') and a long ejector (referred to as 'eject_r1x2'), as shown in Fig. 14. The goal was to determine which of the two ejector concepts would have the least influence on the HWB aerodynamic performance during wind tunnel testing.

Similar to the sting selection study, delta surface pressure coefficient (ΔC_p) plots were used to compare the influence of the two ejector configurations against a baseline configuration. However, it should be noted that due to an oversight the ejectors simulations were generated with the addition of a baseline leading edge Krueger flap which was part of the planned configuration buildup. Furthermore, the project was under a deadline to down select to a preferred ejector configuration and so rather than running additional CFD of the HWB with the Krueger only for the baseline, it was determined that the HWB simulations with the 'short forward' sting from the sting study would be sufficient for use as the baseline. This meant that the ΔC_p results would include influences due to both the ejector configuration and the Krueger flaps as shown by the high ΔC_p s on the wings in Figs. 15. In order to remove the effect of the Krueger, ΔC_p contours were generated between the two ejector solutions ($\Delta C_p = C_{p_eject_r1} - C_{p_eject_r1x2}$) as plotted in Fig. 16. These contours showed that the net ejector influence occurred on the upper surface of the HWB beneath the ejectors and that the short ejector created higher pressure coefficients as indicated by the red contour levels

in Fig. 16 and were consistent with the higher pressures at the same location for the short ejector as shown in Fig. 15a. This higher pressure trend was attributed to the downstream movement of the tapered section for the long ejector (see Fig. 14). Based on these findings, the recommendation was to use the long ejector for all the wind tunnel ejector entries.

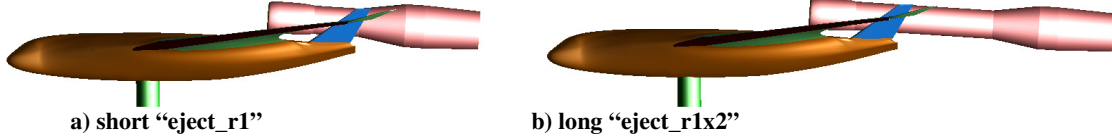


Figure 14. HWB wind tunnel ejector configurations considered.

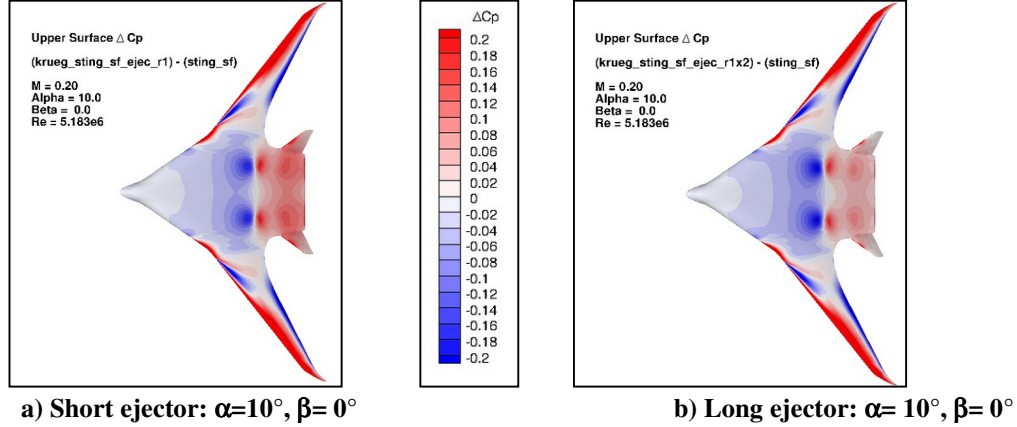


Figure 15: OVERFLOW ejector configuration upper surface ΔC_p =(Ejector_Config.– Clean).

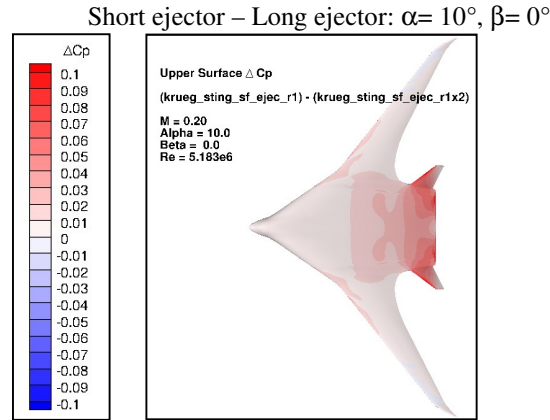


Figure 16. OVERFLOW Upper surface ΔC_p between the two ejector configurations ΔC_p =(eject_r– eject_r1x2).

C. Trip Dot Selection and Placement

The wind tunnel test program was designed to investigate low-speed configuration aerodynamics of the HWB under takeoff and landing conditions, and these included typical high angles of attack and sideslip that can result in separated flow on the vehicle. Effective tripping of the wind tunnel model boundary layers is critical to creating turbulent flow over most of the model at the wind tunnel test conditions ($M = 0.2$, $R_{\text{cref}} = 5.27 \times 10^6$). One particular concern was the effective tripping of the boundary layers that traverse the highly-swept and blunt inboard portion of the HWB configuration. Flow from this area continued over the body upper surface towards the engines, and any flow separations could have important PAI consequences. Therefore, laminar or transitional flows on the body of the wind tunnel model could result in measurements that do not accurately represent full-scale vehicle performance.

Two CFD codes were used to guide the placement and sizing of transition-forcing boundary-layer trip strips for this experiment. Validated CFD transition prediction technology for configuration aerodynamics is not well

established, and a hybrid analysis approach was adopted. The first part of the analysis was focused on determining the forced-transition strip location, and fully turbulent simulations from the unstructured code USM3D²¹ with the SA turbulence model¹³ were used. This analysis focused on the longitudinal onset of adverse pressure gradients, and trip locations were identified slightly upstream of these locations. The second part of the analysis was focused on determining trip-dot heights, and transitional simulations from the overset code OVERFLOW⁴ with the Langtry-Menter transitional boundary-layer model¹⁵ were used. These solutions provided laminar boundary layers in the proposed trip-strip region, and these boundary layers were interrogated to guide the trip-dot sizing. Details from the OVERFLOW/LM simulations showed it predicted the transition front to be downstream of the trip locations determined from the USM3D/SA analysis. This provided good confidence that the location determined by USM3D/SA were conservative. Two trip patterns resulted from this analysis, one for low to moderate angles of attack, and the other for moderate to high angles of attack. Both patterns were comprised of segmented straight lines with fixed dot heights on any one segment. The trip dots were thus very practical to put on the model. The change from the low- α to the high- α patterns coincided with a major model hardware change, so the impact on tunnel schedule was small.

Infrared thermography was used to verify the trip effectiveness as shown in Fig 17, and the tripping was adopted for the test campaign in the LaRC 14'x22' and ARC 40'x80' low-speed wind tunnels. A few photographs of the trip dots on the model are shown in Figure 18.

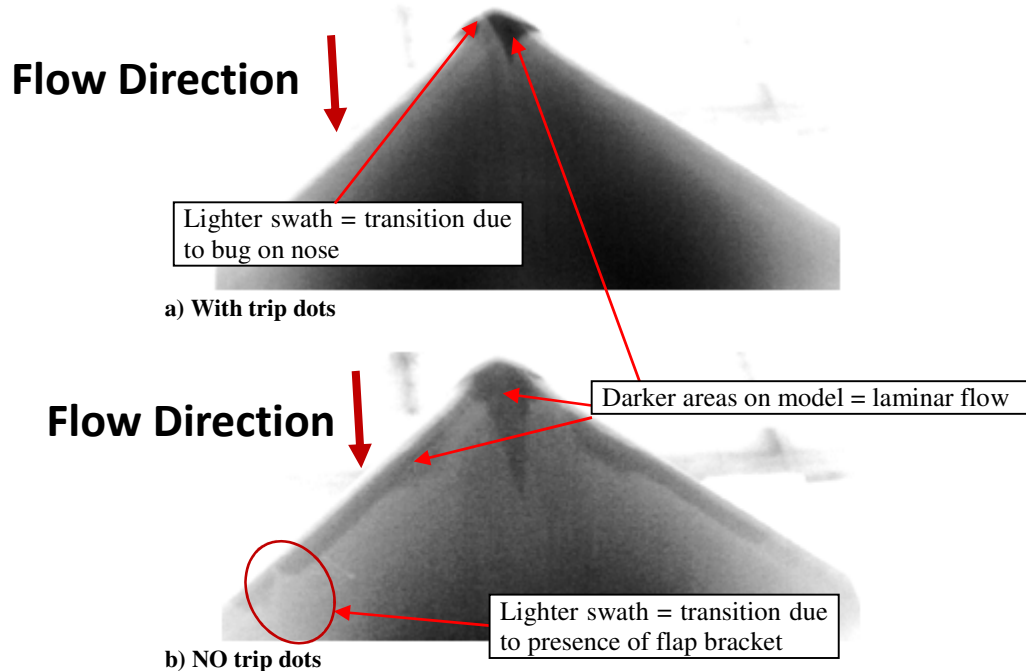


Figure 17. Experimental thermal images of trip dots effectiveness on HWB (from above and behind model)

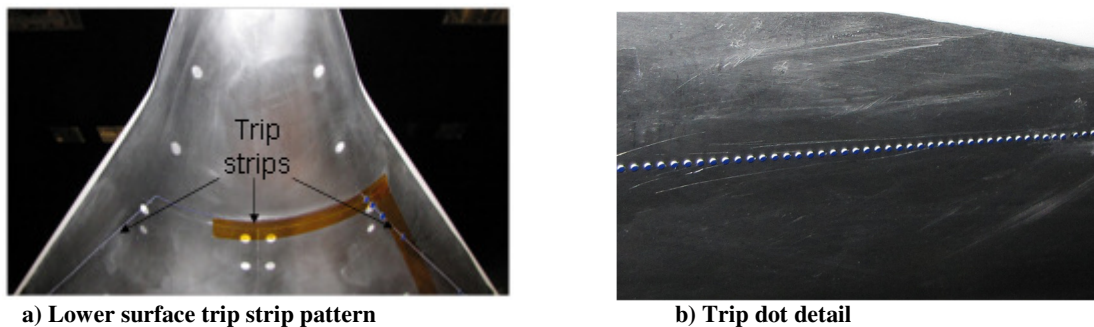


Figure 18. Trip dot application to the ERA/HWB model in the 14'x22' wind tunnel.

D. Aeroacoustic Array Placement and Configuration Assessment

A key system level metric of the project was to demonstrate reduced component noise signatures that would contribute to a 42 EPNdB Stage 4 noise margin for the aircraft system²³. No direct acoustic measurements of the HWB model were originally planned as part of the test program, as all of the noise estimates were to be done computationally. However, the re-planning of the project to the NFAC 40'x80' wind tunnel (after the main drive failure in the 14'x22') afforded an opportunity to acquire experimental acoustic data to better refine noise estimates. A new traversing array support was proposed for installation below the portside wing of the HWB in order to measure Krueger flap noise for a number of configurations (Fig. 19). The array support was proposed because the floor of the 40'x80' test section was thought to be too far from the model for accurate noise measurements. A post was used to support the placement of a 50"x80"x4" acoustic array underneath the portside wing, and a computational effort was undertaken to assess and help minimize the aerodynamic influence of the acoustic array mounted in proximity to the wind tunnel model. Three vertical and three horizontal array placement options were analyzed. The following three vertical locations were considered: 1) 24" below the portside wing, 2) 48" below, and 3) 96" below the portside wing. These vertical positions are depicted in Fig. 19. A single vertical height was selected from these three options and then three horizontal locations were evaluated based on three directivity angles of 60°, 90° and 120°. The 90° directivity angle located the array directly below the reference point underneath the wing, while the 60° angle is forward of the wing, and 120° angle is aft.

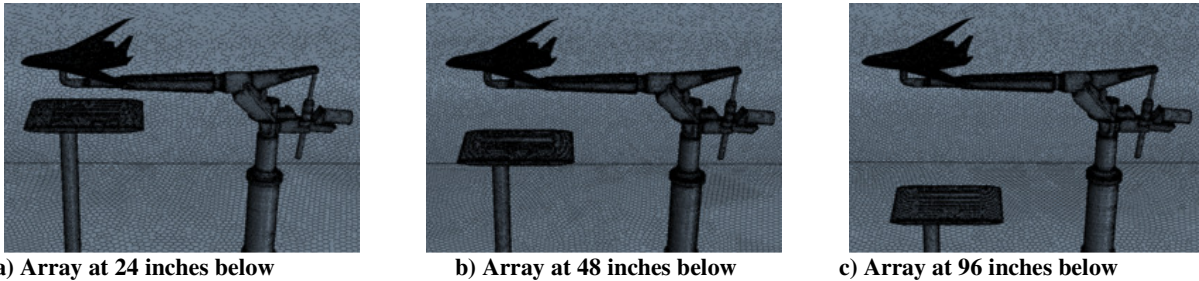


Figure 19. Acoustic array vertical placement considered for 40'x80' WTT.

STAR-CCM+ flow simulations were used to compute the force and moment increments caused by the vertical acoustic array, using the no array solutions as the reference case. These simulations included all of the associated support structure and 40'x80' wind tunnel walls. STAR-CCM+ was used due to its ability to rapidly generate and assess the many geometries being considered for the various acoustic array assembly locations. The resulting flow field predictions were used by the experimentalists to guide the wind tunnel model design setups in the 40'x80' wind tunnel. The CFD results showed that the force and moment coefficients were generally unaffected by the array at the 48" and 96" vertical locations, as shown in Fig. 20. The pitching moment showed the most sensitivity to array post height. When the acoustic array was placed at the 24" separation location, there was a marked change in the pitching moment. At the 48" location, that increment appeared to be acceptably small. At the 96" location, no increment was present when compared to the no-array results. These predictions were consistent with the measured pitching moments from the wind tunnel test as shown in Fig. 20b. Note, the axes of both plots in Fig. 20 use the same minimum and maximum values for angle of attack and pitching moment coefficient.

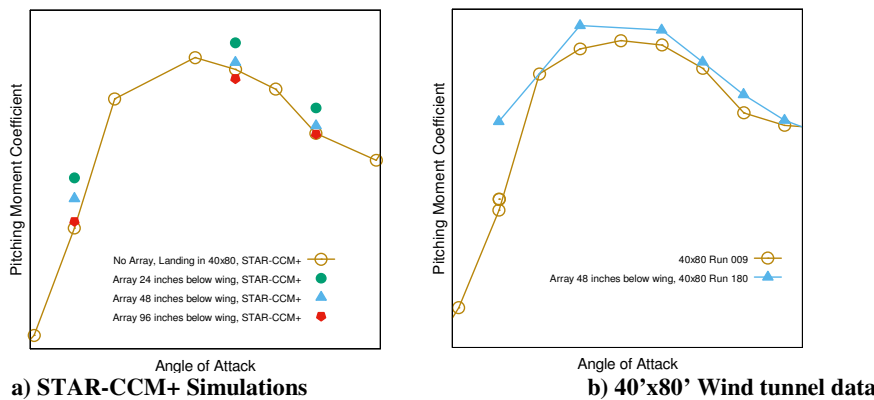


Figure 20. Vertical array placement effect on HWB pitching moment.

In order to take a closer look at the influence of these array locations on the HWB, sectional surface pressure coefficient at various span wise locations were compared to those without the array for the 24” and 48” vertical array separations, as shown in Figs. 21 and 22. These results showed slight differences in the pressures around the leading edge Krueger flap and the main wing for the 24” array location (Fig. 21). At the 48” position the pressures are nearly identical, as shown in Fig 22. From these results, the project selected the 48” position as the optimal separation distance of the array support platform from the model and used this position for the directivity angle selection analysis.

In order to evaluate the horizontal placement of the array, the FUN3D flow solver was run at NASA Ames Research Center, using the three directivity angles of 60°, 90° and 120° configurations. FUN3D meshes were obtained using the STAR-CCM+ polyhedral surface meshes, which were converted into surface triangles using Pointwise and then prismatic volume meshes were generated using AFLR. This enabled the CFD group to apply two different CFD solvers on the same problem simultaneously using similar meshes, and providing a good opportunity for code-to-code comparisons.

The 60°, 90° and 120° directivity angle acoustic array locations at 48” below the portside wing are shown in Figs. 23, 24 and 25, respectively. Also include in these figures are surface contours plots of delta pressure coefficients (ΔC_p) between the given array location solution and the no-array baseline solution predicted by FUN3D. In order to closely investigate the influence of these array locations on the aerodynamics of the HWB, sectional surface pressure coefficient distributions at various span wise location were compared to those without the array for the 60°, 90° and 120° acoustic array locations, as shown in Figs. 26, 27, and 28. These figures indicated that there was no significant influence on the surface pressures due to the array locations. All of the C_p distributions appeared to be identical to the no-array baseline pressure distributions. Armed with this information, the experimentalists and acousticians were able to proceed with confidence, knowing that the acoustic array placed 48” below the portside wing at the three directivity angle locations should not affect the flow around the HWB.

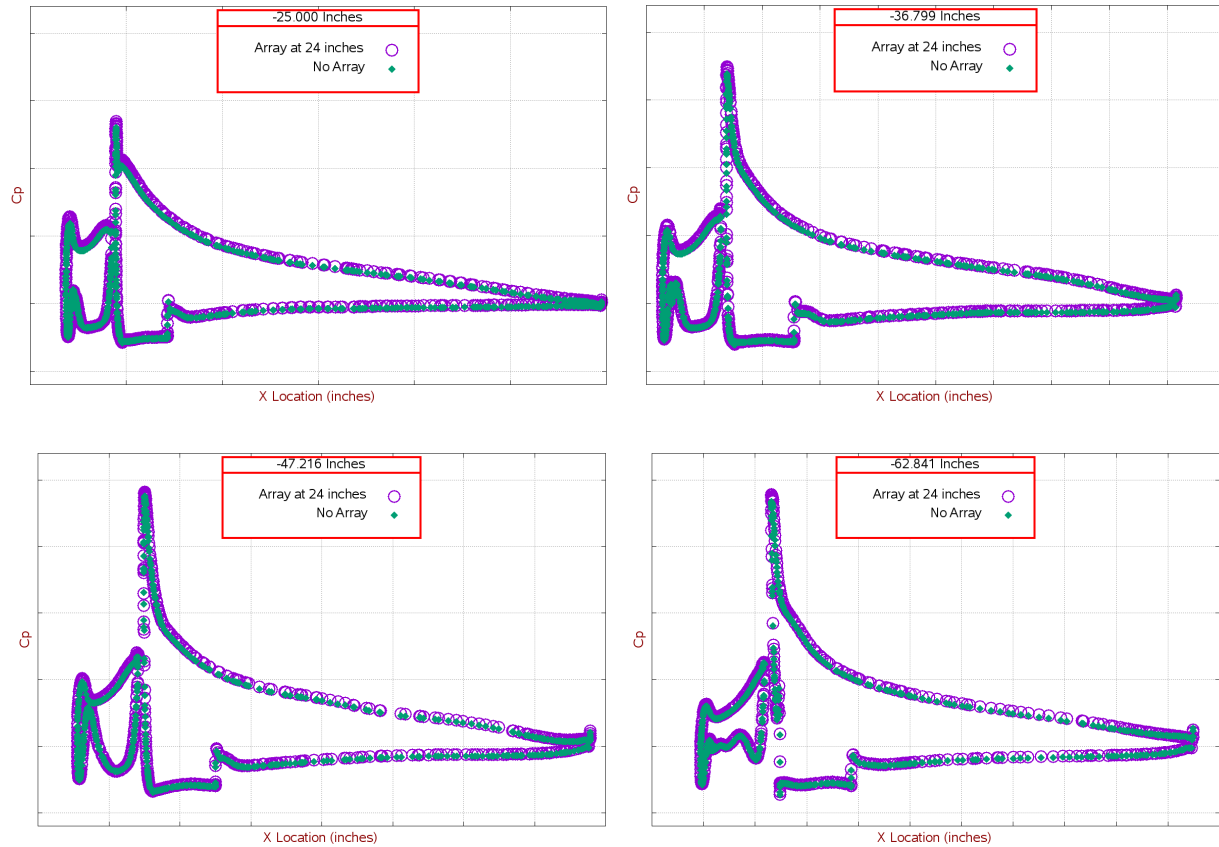


Figure 21. Star-CCM+ wing sectional C_p with array 24” below and without array at $\alpha=12^\circ$.

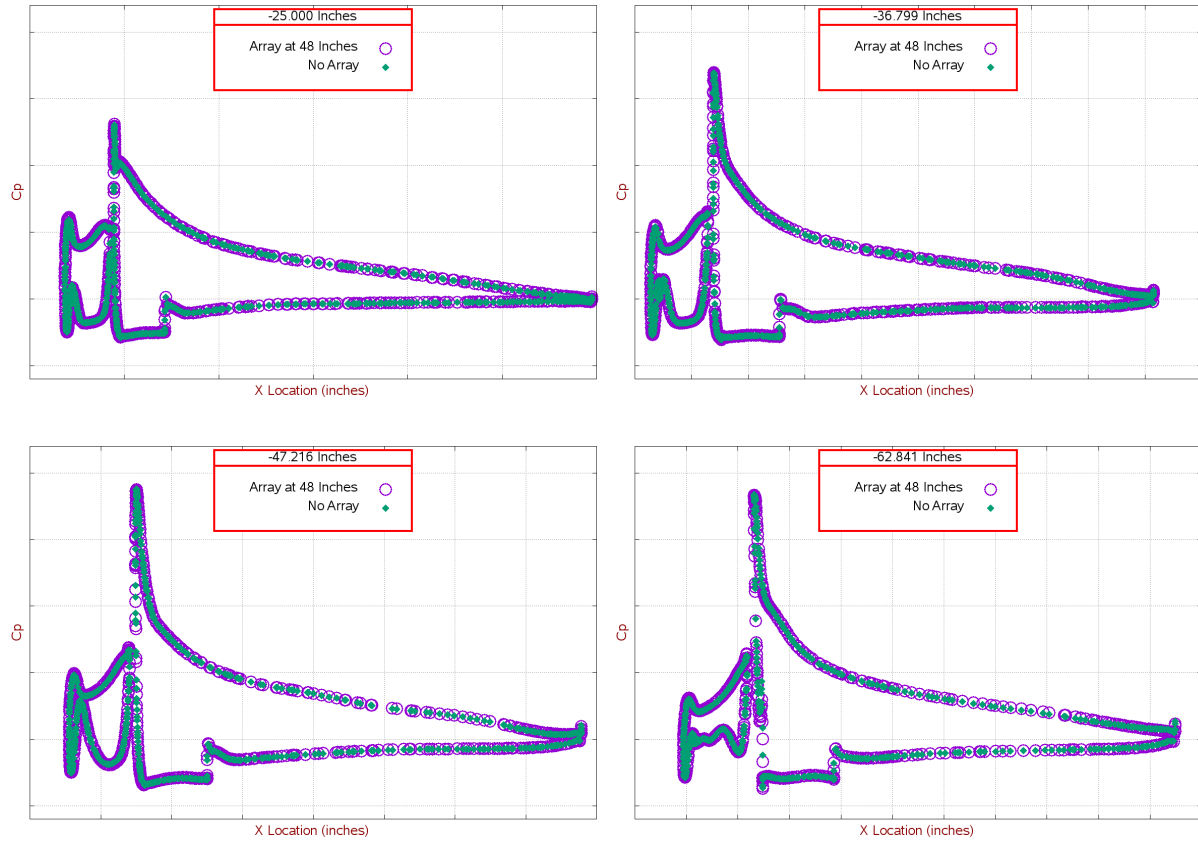


Figure 22. Star-CCM+ wing sectional C_p with array 48" below and without array at $\alpha=12^\circ$.

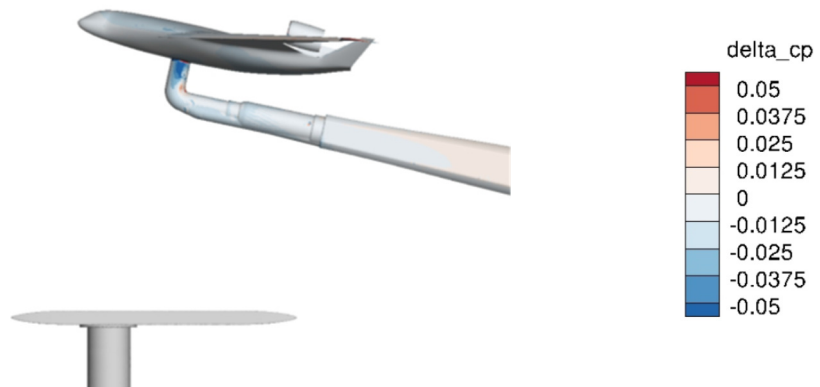


Figure 23. FUN3D 60° array placement surface $\Delta C_p = (\text{Array}60^\circ - \text{noArray})$ at $\alpha=12^\circ$, $\beta=0^\circ$.

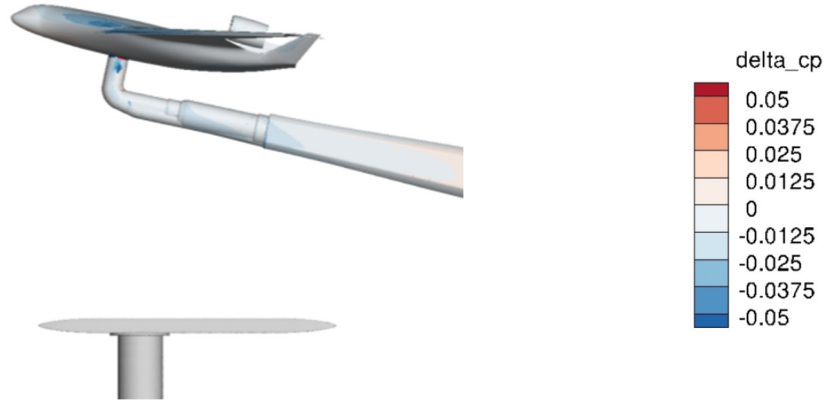


Figure 24. FUN3D 90° array placement surface $\Delta C_p = (\text{Array90}^\circ - \text{noArray})$ at $\alpha = 12^\circ$, $\beta = 0^\circ$.



Figure 25. FUN3D 120° array placement surface $\Delta C_p = (\text{Array120}^\circ - \text{noArray})$ at $\alpha = 12^\circ$, $\beta = 0^\circ$.

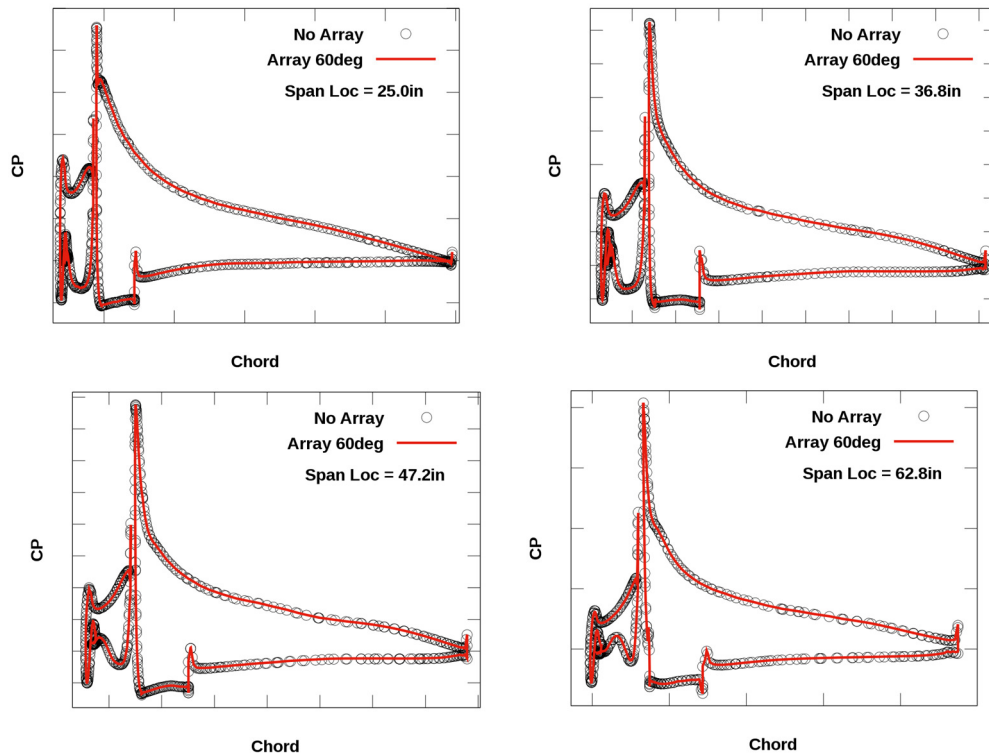


Figure 26. FUN3D 60° array sectional C_p portside wing comparisons at $\alpha = 12^\circ$, $\beta = 0^\circ$.

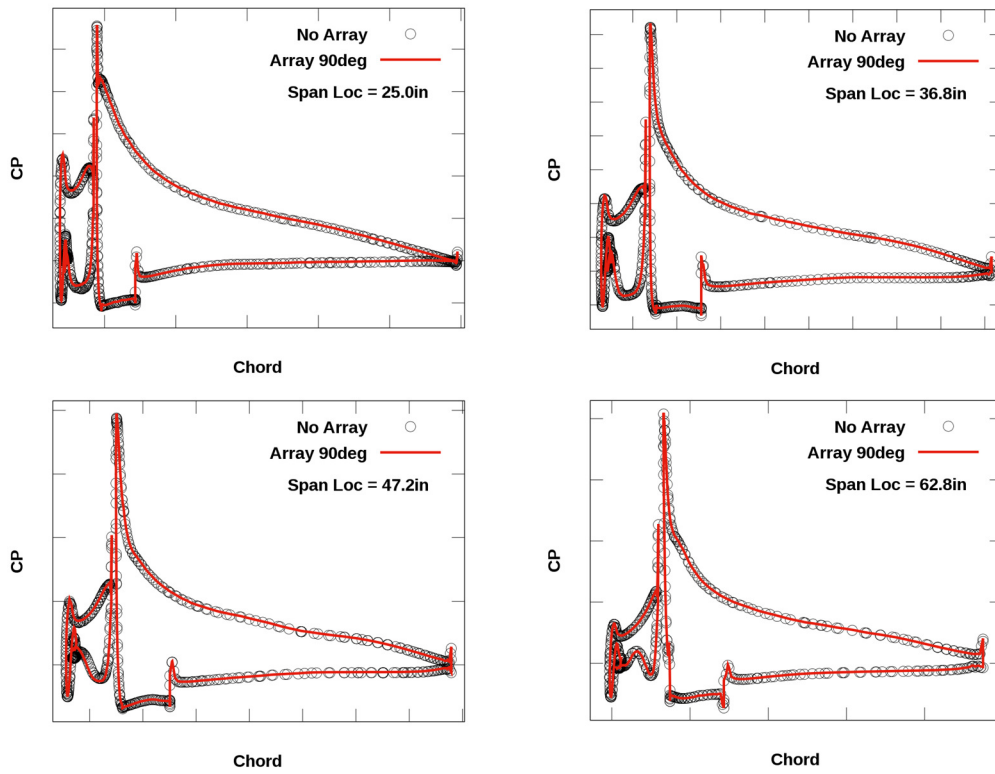


Figure 27. FUN3D 90° array sectional C_p portside wing comparisons at $\alpha=12^\circ$, $\beta=0^\circ$.

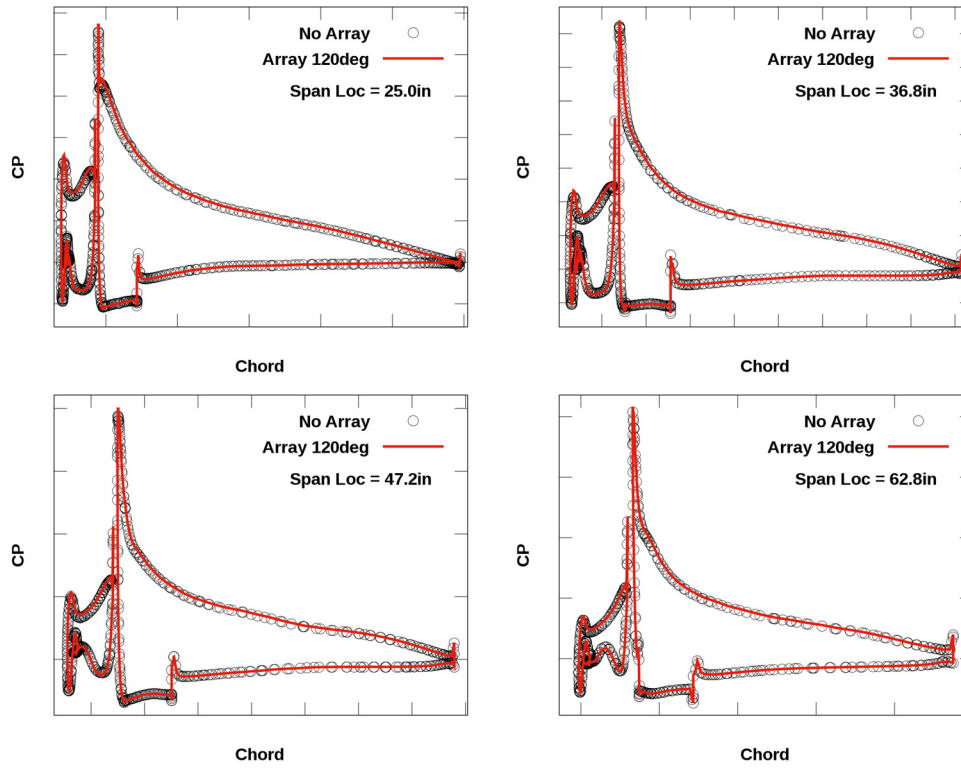


Figure 28. FUN3D 120° array sectional C_p portside wing comparisons at $\alpha=12^\circ$, $\beta=0^\circ$.

E. Sting Installation CFD support

One of the key aspects of this project was that both the wind tunnel experimentalists and the CFD analysts worked side-by-side through the entire project. This made for a well-informed team with firsthand knowledge of everything from test setup and the intricacies of data measurements, to the details of various wind tunnel correction strategies for processing the data for post-test comparisons with CFD.

One example of this type of close collaboration was demonstrated during the 40'x80' model setup, when it was observed that the sting collar adapter used to mate the model sting to the 40'x80' mounting hardware produced a large diameter step increase as shown in Fig. 29. Because experimentalist had CAD available, the CFD group was able to perform simulations to show the impact of this step on the flow field about the HWB model.

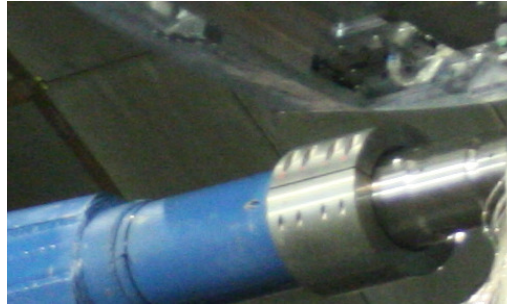


Figure 29. Initial sting adapter installation in the 40'x80' wind tunnel entries.

Simulations using the STAR-CCM+ flow solver for the sting adapter based on the following configurations were performed: 1) the original step collar, 2) a faired collar developed with the STAR-CCM+ geometry tool, and 3) no collar shown in Fig 30. Figure 31 shows the effect on pitching moment due to the three collar configurations. The original step collar solution produced higher pitching moments with a sharp increase at high angles of attack as compared to the no collar result. The pitching moments from the faired collar solutions overlaid the no collar results up to fairly high angles of attack. These results provided the motivation that there was a need to fair the sting transition into the 40'x80' strut mount assembly. Fig. 32 shows how the experimentalists achieved this.

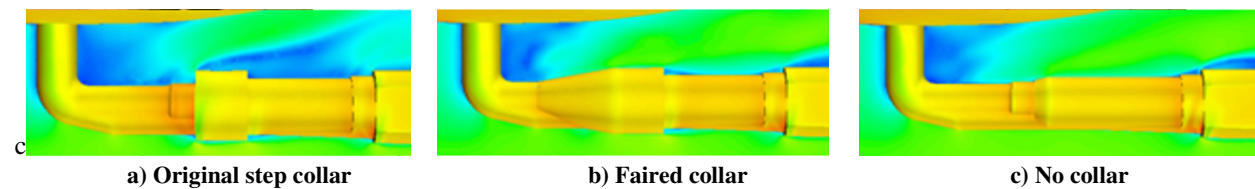


Figure 30: Sting collar adapter installation study for the 40'x80' wind tunnel entries.

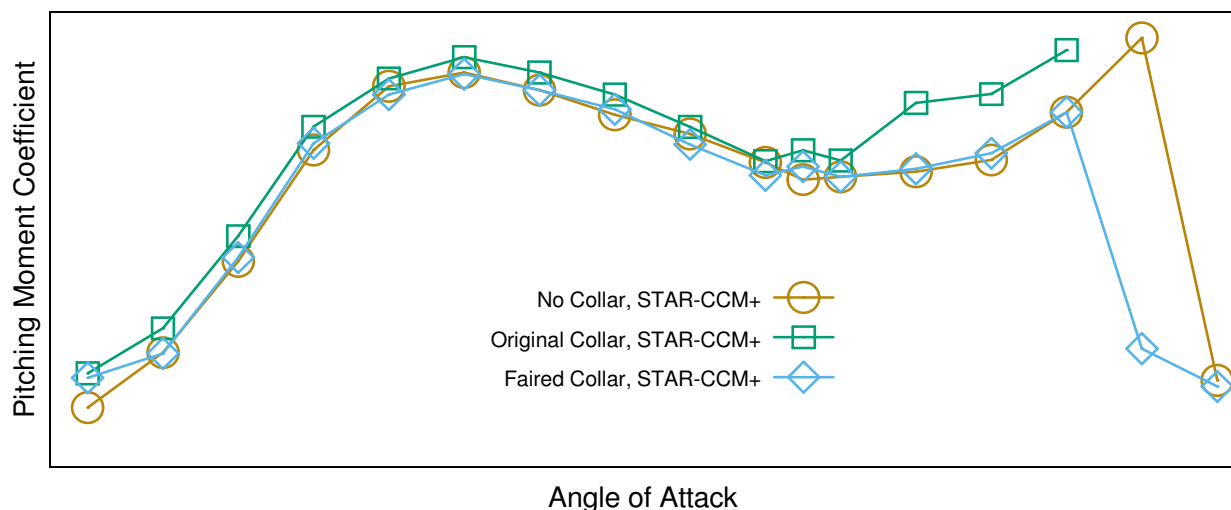


Figure 31. Star-CCM+ 40'x80' faired collar pitching moment comparison.



Figure 32. Final sting adapter with faired collar installed in the 40'x80' wind tunnel.

F. Wind Tunnel Wall Corrections

Pre-test CFD analysis was conducted to explore and compare the “classic” wind tunnel test corrections with CFD-based predictions of the tunnel installation effects. The “classic” corrections were applied to correct for blockage effects, buoyancy effects, strut interference effects and stream curvature effects^{24,25}. Both the CFD-based corrections and the classic corrections used the same correction methodology and equations. Only the correction parameter values differed. The CFD-based parameter were established based on a least-squares fit of the parameter values that best matched the CFD-predicted corrections. The CFD-based corrections were only available for the 14'x22' tunnels results.

A series of tests of the same HWB model configuration in the 14'x22' tunnel with the open and closed test section provided an opportunity to compare the classic and CFD-based corrections. The correction methods are intended to correct the data for tunnel installations effects and provide “free-air” aerodynamic measurements. The corrected data from the open and closed tunnel measurements of the same model configuration should therefore overlay each other. Figure 33 shows a comparison of uncorrected longitudinal force and moment data from a series of open and closed test sections experimental runs with the same landing Krueger model configuration. The differences are most evident in the lift and drag at the higher angles of attack.

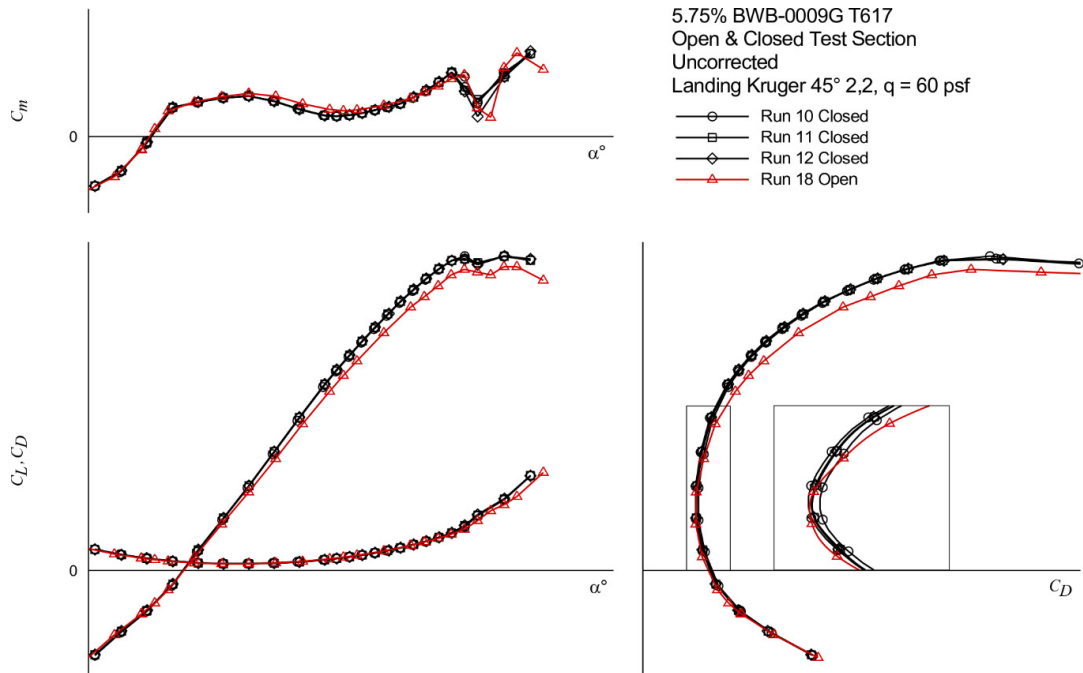


Figure 33. Comparison of uncorrected open- and closed-tunnel longitudinal force and moment data for a landing Krueger configuration.

Figures 34 and 35 show the same data sets corrected with the classic and CFD-based values, respectively. Both methods provide an improvement in the matching of the open and closed tunnel measurements. The CFD-based corrections were expected to provide a better match than the classic method. A closer examination of the matching is

provided in Fig. 36, which shows the difference from the average of the three closed test section runs. Figure 36 also shows that the match provided by CFD-based corrections was no better and in some cases slightly worse than

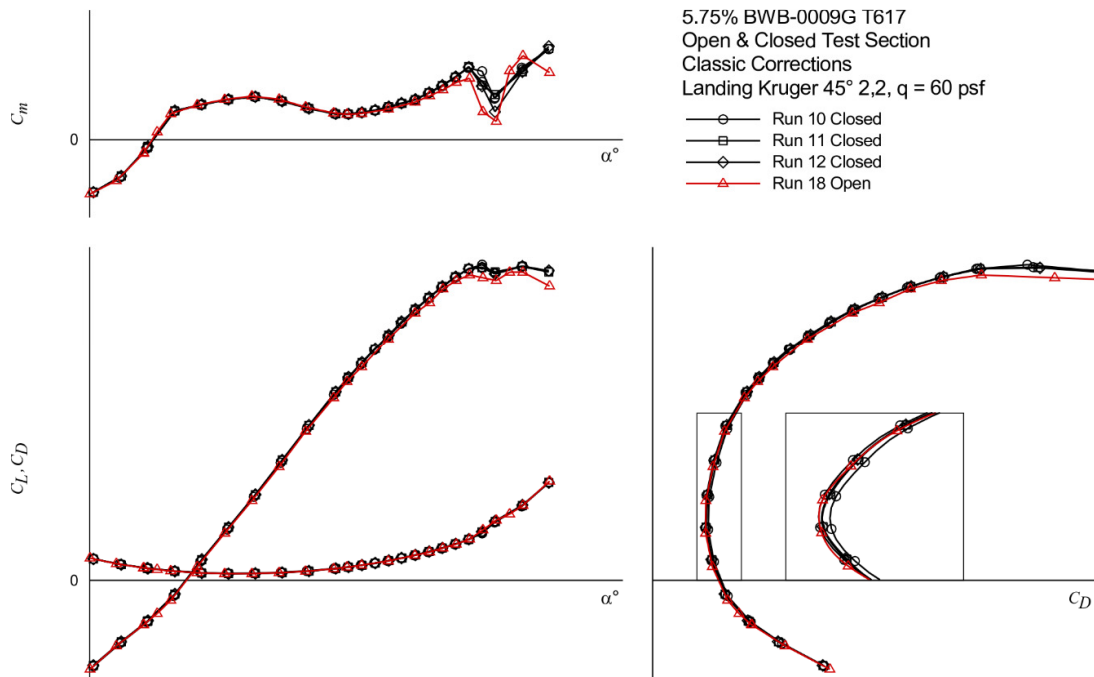


Figure 34. Comparison of classic corrected open- and closed-tunnel longitudinal force and moment data for a landing Krueger configuration.

the classic corrections. Additional post-test CFD analysis including the NFAC test configuration comparison should provide greater insight into the test corrections and is worthy of further investigation.

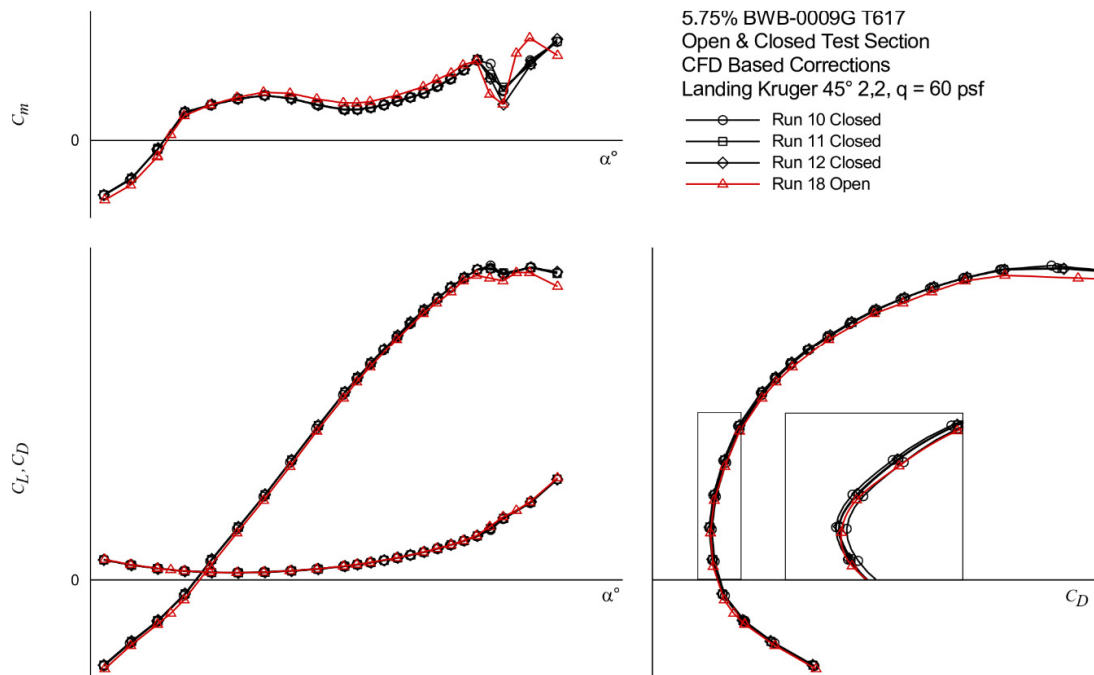


Figure 35. Comparison of CFD corrected open- and closed-tunnel longitudinal force and moment data for a landing Krueger configuration.

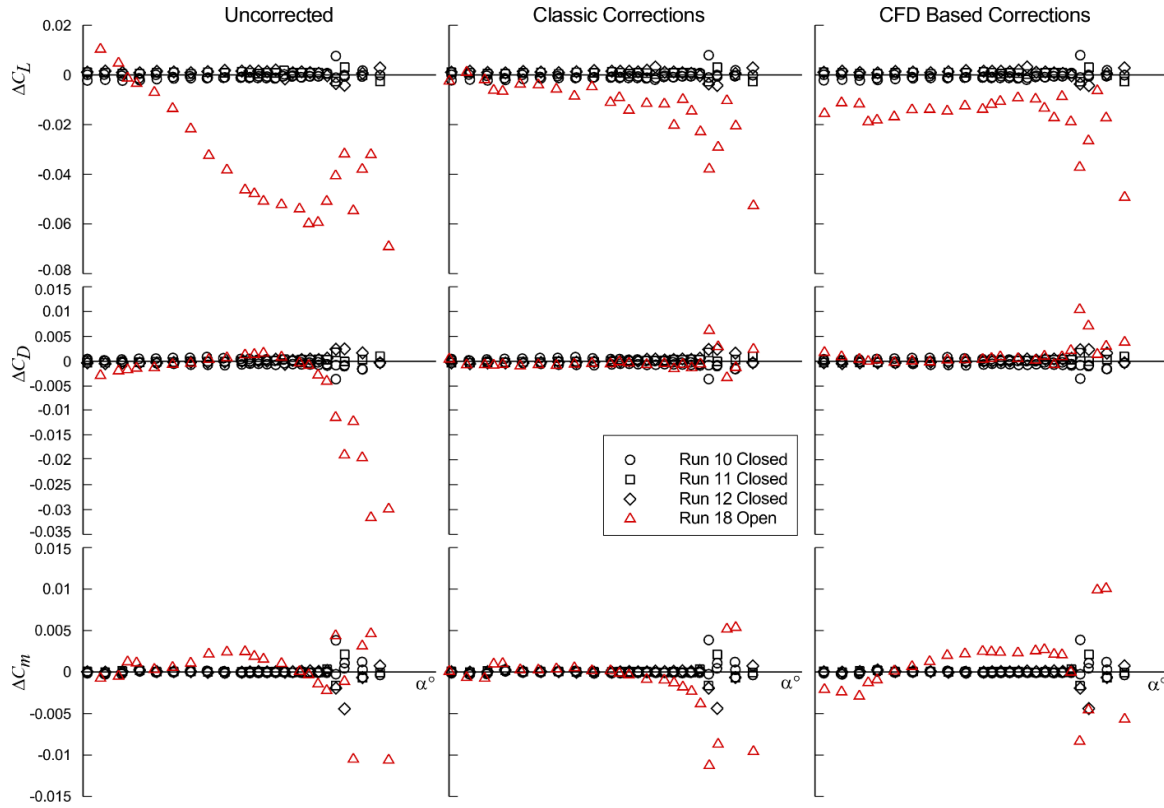


Figure 36. Comparison of the difference from the average of the three closed test section runs.

IV. Lessons Learned and Simulation Guidelines

The following section highlights a few of the most important lessons learned during the execution of the CFD wind tunnel support efforts.

A. Support Post Unsteadiness

Complex mounting hardware geometry, such as the 40'x80' wind tunnel sting assembly shown in Fig. 37a, can result in unsteady, separated flow during a wind tunnel test. This unsteadiness can require computationally expensive, time accurate simulations, which may not actually influence the mean aerodynamics of the configuration of interest. Therefore, introducing simplifications to the geometry being simulated in order to eliminate unsteadiness in the flow solutions due to certain geometric features can greatly reduce computational expense without impacting the accuracy of the predicted mean aerodynamic quantities of the model. A good example of this was the modeling of the HWB with the 40'x80' model support system, which included a large diameter vertical post as shown in Fig. 37a. CFD modeling of this original support post configuration (Fig. 37a) with FUN3D showed a low-level unsteadiness in the lift coefficient at 12 degrees angle of attack as shown by the solid blue lines of Figs. 38 and 39. Preliminary assessment indicated a large unsteady wake behind the post.

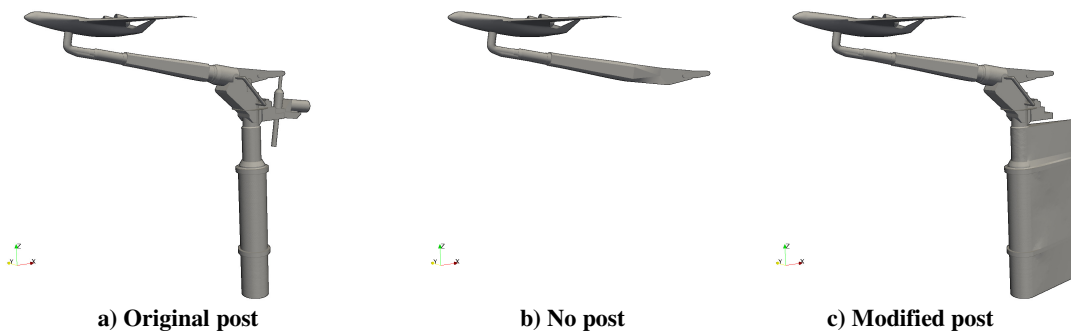


Figure 37. 40'x80' post geometry simplification.

Without the post, at these same conditions, the simulated HWB flow did not exhibit this type of unsteadiness. In order to simplify the problem, the post was removed (as shown in Fig. 37b) to determine if averaged integrated loads would be affected. FUN3D simulations of this ‘no-post’ configuration showed a reduction in lift and an increase in drag, as shown by the red dashed lines in Figs. 38 and 39, respectively. This was attributed to changes in the flow around the HWB due to reduced blockage when the post was removed. As an alternative to removing the post, a faring was added around the post in the CFD simulations as shown in Fig. 37c. It should be noted that the wind tunnel vertical post was spiral-wrapped with a thick rope to disrupt coherent Strouhal shedding. The CFD geometry modification was designed to achieve a similar end goal, via an alternate mechanism. The modified post maintained the blockage effect but lessened the bluff body unsteady separated flow behind the post. In addition to the faring, the complex geometry of the motor and jack screw mechanisms behind the sting were also removed.

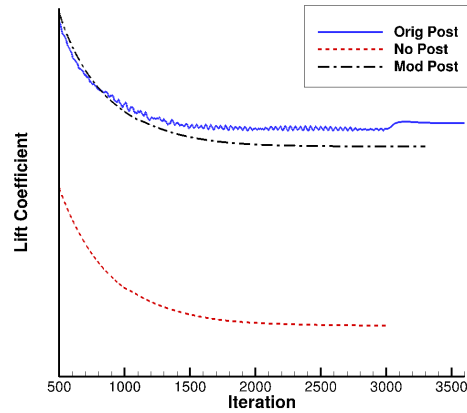


Figure 38. FUN3D HWB lift coefficient comparisons due to 40’x80’ post geometry simplification at $\alpha=12^\circ$.

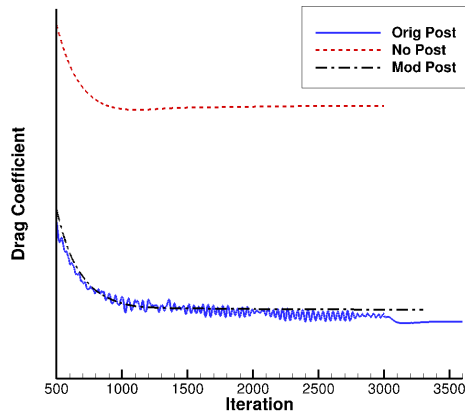


Figure 39. FUN3D HWB drag coefficient comparisons due to 40’x80’ post geometry simplification at $\alpha=12^\circ$.

These geometric modifications enabled FUN3D to converge to a steady state solution using the non-time-accurate mode and provided mean aerodynamic lift and drag coefficient that were within 0.5% of the averaged time-accurate simulation. Furthermore, this non-time accurate steady state solution was approximately 50% of the computational cost required by the time-accurate solutions. Table 1 lists the differences in the aerodynamic lift and drag coefficients. The ‘No post’ solution translated into an increase in drag of ~23 drag counts, while the modified post showed approximately a 1.3 drag count increase. These drag differences can be significant when using CFD results to guide

Table 1. Effect of model support post modifications on CFD lift and drag predictions.

	$\Delta CL\%$	$\Delta CD\%$	$\Delta \text{Drag count}$
no post	-4.6%	6.4%	23.3
modified post	-0.53%	0.35%	1.3

the extrapolation from wind tunnel data to flight. These geometry modifications also enabled FUN3D to conduct angle of attack and sideslip angles sweeps below stall with a non-time-accurate approach saving both CPU and wall clock time.

B. High angle of attack CFD flow predictions

An issue in CFD prediction accuracy emerged in the simulations of the flow near the onset of stall. The following comments are based on FUN3D results at an angle-of-attack of 20 degrees using the SA turbulence model. However, similar simulation results were obtained with Star-CCM+ using the SST turbulence model and with OVERFLOW using the SA model.

Measurements of the HWB wind-tunnel model in the high-lift landing configuration with Krueger flaps deployed (Fig. 40a) indicated that boundary layer separation occurred on the upper surface of the wing at relatively high angles of attack, as shown by the slope change in the pitching moment and sudden decrease in the lift curves of Figs 33, 34 and 35. However, CFD solutions typically predicted that separation occurred at lower angles of attack.

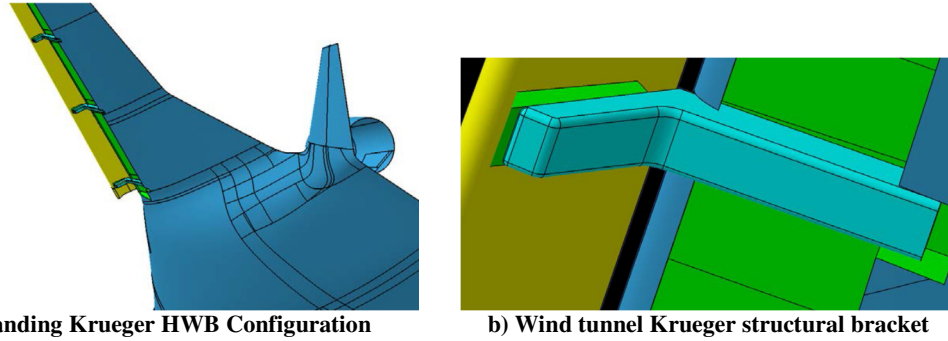


Figure 40. Landing Krueger and close up view of structural bracket [from Ref. 2].

Analysis of the CFD solutions revealed a significant dependence of the flow separation on the time-integration process. Solutions using the non-time accurate scheme, with simple spatially variable time stepping, tended to compare better with experimental measurements, but they approached an asymptotic state with low-level unsteadiness, as shown in Fig 41a. Experience from prior CFD analyses indicates that time accurate integration should be used in these cases. Therefore, additional solutions were computed using the second-order backward difference, time-accurate scheme, with a reasonably small time step and sufficient inner iterations to achieve good sub-iteration residual convergence. These time-accurate simulations resulted in large separation downstream of the Krueger brackets (Fig. 40b), resulting in approximately a 10% change in the integrated loads, which greatly diminished their accuracy in comparison to the experimental measurements as shown in Fig. 41b. Similar behavior was also observed in simulations performed at ARC using Star-CCM+ and OVERFLOW. Note, the lift coefficient y-axes of both plots in Figs. 41 use the same minimum and maximum values.

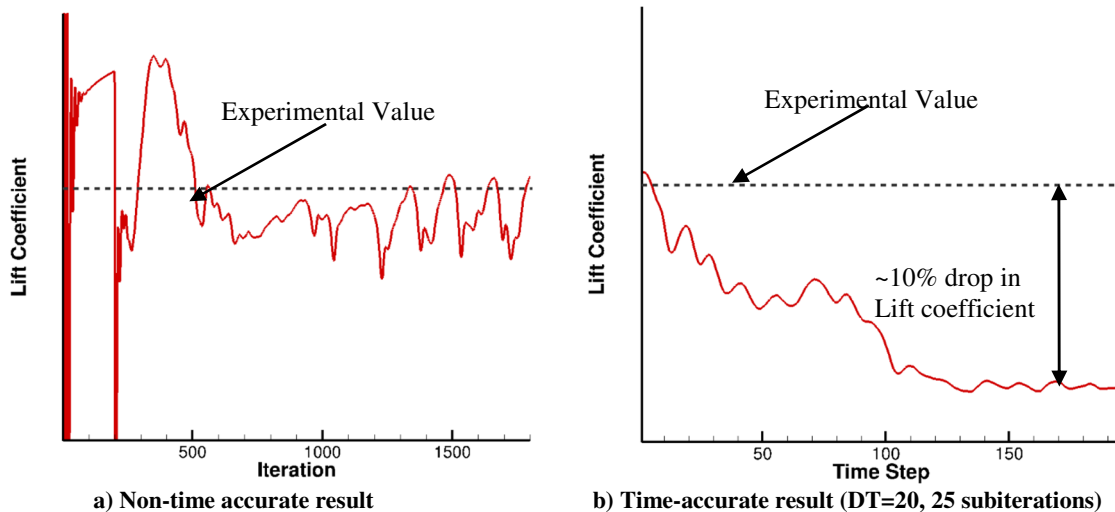


Figure 41. FUN3D lift dependency on time integration process for HWB landing configuration at $\alpha=20^\circ$.

A proposed explanation for the non-time-accurate result was that it created "resolved pseudo-turbulent" stresses that suppressed the separation bubble, and kept the flow attached. Unfortunately, this resolved pseudo-turbulence was computed with an algorithm that lacks time accuracy; thus, the pseudo-turbulence was not physical. The strategy for understanding the issue was to pursue a truly time-accurate solution, which could be used as a "truth" solution for judging temporal inaccuracy in other solutions. The spatial discretization error was considered to be a constant, and assumed to not invalidate this approach. Results of this study are given in Fig. 42 using the following four CFD time steps: 1) $DT=0.02$ with 3 subiterations, 2) $DT=5.0$ with 50 subiterations, 3) $DT=10$ with 100 subiterations, 4) $DT=10$ with 20 subiterations.

The rationale used to select these CFD time steps was to express them in terms of a physical vortex shedding Strouhal number (St) of 0.25. This was done since the nominal Strouhal number of many unsteady separated wake flows tends to fall into a small range between 0.15 and 0.25²⁶. Further, the Strouhal number is defined as: $St = fL/U$. Where, f is the frequency, L is the relevant length scale, and U is the relevant velocity. In order to express St in terms of a CFD time step (DT), the Strouhal number equation is rewritten such that the frequency $f=1/DT$, and the velocity U is set to freestream (U_∞). In FUN3D, the time step is normalized by the sound speed. This will then yield what is referred to as the time step based Strouhal number (St_{DT}) as follows: $St_{DT} = L/(DT*M_\infty)$ in terms of the FUN3D grid units. Next, the ratio of the time step Strouhal number (St_{DT}) to the physical Strouhal number (St) is used as a coarse measure of time integration accuracy. For good time accuracy, this Strouhal ratio, St_{DT}/St must be at least 20, as the second-order backwards-difference time-integration scheme requires roughly that many points per period assuming a simple sinusoidal oscillation for high accuracy. An even higher ratio is needed if any part of the unsteady flow changes more rapidly than the gross features like integrated loads, and this is very common. Thus, the ratio of Strouhal numbers, St_{DT}/St should be 20 or greater, by an unknown amount, to achieve good time accuracy.

The implication of time accuracy then depends on the relevant length scale in the region of interest. Two examples relevant to this study at $M_\infty = 0.2$ are discussed, and others can be constructed similarly. For the Krueger structural brackets (Fig 40b), with a reference length of $L = 0.6''$, and a time step of $DT = 1$, the $St_{DT} = 3$. This yields a Strouhal ratio $St_{DT}/St = 12$, assuming a vortex shedding $St = 0.25$, which is a low ratio value and is likely to have poor time accuracy. At a $DT = 10$, the time step yields a $St_{DT} = 0.3$ which nominally matches the bracket's vortex shedding frequency ($St = 0.25$) and yields a Strouhal ratio $St_{DT}/St = 1.2$, which would destroy any time accuracy around the Krueger structural bracket HWB's aerodynamics. A second phenomenon of interest is unsteadiness in the separation bubble which was observed to form on the wing's upper surface, and nominally had a characteristic reference dimensional length of $L \sim 10''$. In this case, a time step of $DT = 1$ gives $St_{DT} = 50$ and $St_{DT}/St = 200$, which suggest that this $DT=1$ would provide very good time accuracy; at $DT = 10$, $St_{DT} = 5$ and $St_{DT}/St = 20$, which would compromise the time accuracy somewhat, principally in the rapid details of the flow. At a $DT = 50$, $St_{DT} = 1$ and $St_{DT}/St = 4$, therefore any unsteadiness at the nominal physical Strouhal frequency ($St=0.25$) would be extremely damped and unresolved. Based on these principles, several simulations were conducted at a range of time steps as shown in Fig. 42. Simulations were initially run at a $DT = 0.02$ (red line) and $DT = 5$ (blue line) in an attempt to best resolve the smaller scale unsteady shedding directly downstream of the blunt Krueger structural brackets (Fig. 40b). Due to computational and time constraints, these simulations were prematurely concluded and a simulation with a $DT = 10$ (green line) was run until a definite repetitive unsteady behavior was achieved. Note that although the $DT = 0.02$ and $DT = 5$ simulations did not run as long as the $DT = 10$ simulation, the initial lift histories all show excellent agreement. An additional simulation at $DT = 10$ (dashed orange line) was run with 10% as many subiterations as the aforementioned $DT = 10$ simulation to examine the effect of subiteration convergence. The lift coefficient visibly drops by $\sim 10\%$ when 10 subiterations are used at each outer time step. Figures 43a and 43b show the inner iteration residual drop for the $DT = 10$ with 10 subiterations and $DT = 10$ with 100 subiterations simulations, respectively. While typical inner iteration residual convergence of two orders of magnitude could be considered sufficient, as seen in the $DT=10$ with 10 subiterations (Fig 43a), the integrated lift coefficient history results of Fig. 42 demonstrated that this was insufficient. The $DT=10$ with 100 subiteration residuals convergence of Fig. 43b, showed an asymptotic convergence with approximately 4 orders of magnitude drop in residuals, and the integrated lift compared much better with experimental lift results, as shown in Fig. 42.

Another method used to check the accuracy of the outer time step was to verify that the inner iteration forces and moments converged to an asymptotic value. This was done for the total lift force of the HWB computation as shown in Fig. 44a for the $DT = 10$ with 10 subiterations and in Fig. 44b for the $DT = 10$ with 100 subiterations. These results indicated that 10 subiterations appeared to reach an asymptotic convergence, however based on the comparison in Fig. 42, the $DT=10$ with 10 subiterations was insufficient in providing a good comparison with the experimental value. It should be noted that the version of the FUN3D code utilized in this study did not have the option to assess the inner iteration of the viscous force alone which would be much smaller and could provide a better means for verifying the

convergence of the boundary layer for these type of flows. Because of this it was believed that an alternate convergence check for these flows was to verify that the inner iteration of the overall residual reached an asymptotic state as shown in Fig. 43b which required 100 subiterations for a DT=10.

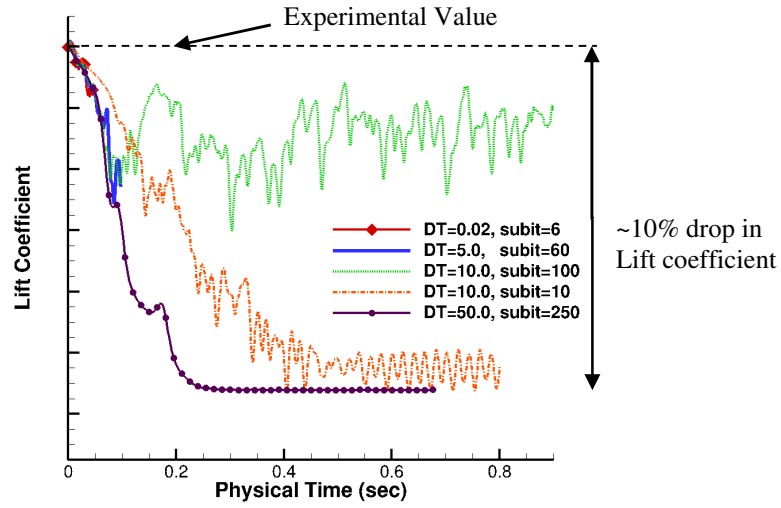


Figure 42. CFD-RANS time accuracy study effect on Lift for the HWB landing configuration at $\alpha=20^\circ$.

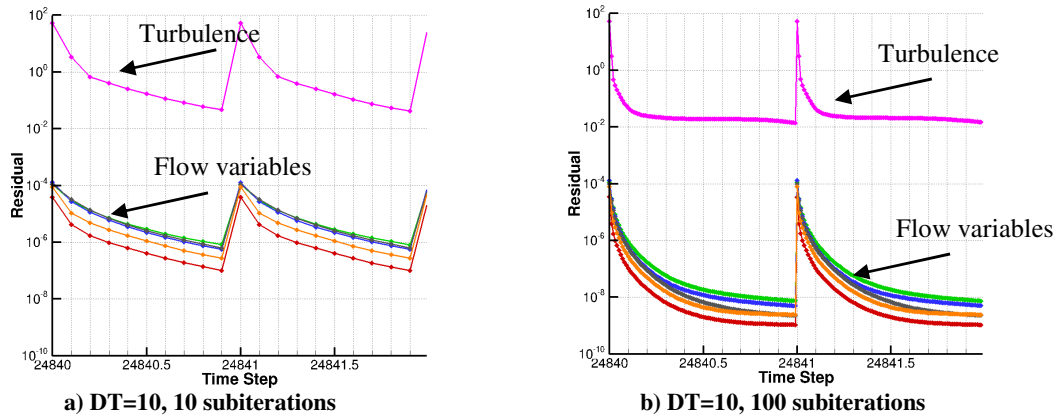


Figure 43. FUN3D Time accurate residual subiteration convergence for HWB landing configuration at $\alpha=20^\circ$.

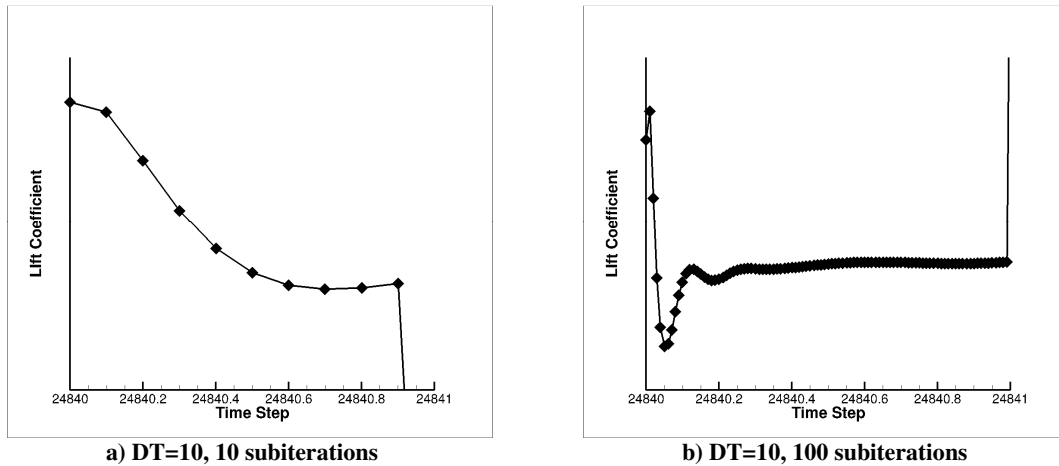


Figure 44. FUN3D Time accurate integrated lift coefficient subiteration convergence for HWB landing configuration at $\alpha=20^\circ$.

In order to better understand how the flow differed between the two $DT=10$ simulations with 10 and 100 subiterations, instantaneous surface streamlines were saved at the end of each simulations as shown in Fig. 45. The blue contours indicate reversed flow in the separated regions. Note, the separation bubble directly downstream of the second and third most inboard structural bracket for the $DT=10$ with 10 subiterations, shown in Fig. 45a, is much larger than the $DT=10$ with 100 subiteration result of Fig. 45b. This larger observed separation bubble based on the 10 subiterations is consistent with the lower integrated lift in Fig. 42.

Finally, another simulation was run with a large $DT = 50$ using first-order time accuracy to forcibly coerced the unsteady separation on the upper surface of the wing along with 250 subiterations to ensure inner convergence. The integrated lift coefficient history of this is shown by the burgundy line with solid circles in Fig. 42. Although a steady state value is achieved, the integrated lift coefficient again was $\sim 10\%$ lower than the experimental value. This result indicates that the standard RANS turbulence models have insufficient accuracy for the complex turbulence physics of the flows considered here when run using standard practices.

These findings indicate that the resolved high-frequency turbulence in the wake of the Krueger support bracket along with the separation bubble that forms on the upper surface of the wing at these high angles of attack are critical to accurately model the upper-surface separation of the wing. Non-time-accurate simulations do not solve the governing equations, and are not reliable for critical unsteady phenomena. Results are acceptable, only if sufficient turbulence is resolved, and the models are operating in a form of RANS-DES mode. Currently, our CFD tools are limited in their ability to predict this flow field using standard turbulence models, and the time-accuracy needed to improve overall simulation fidelity is computationally expensive.

Additional simulations and comparisons with the available experimental data for other similar flight conditions are required in order to provide greater insight into simulating these flows. Fortunately, flight Krueger support brackets are smaller and more numerous than the wind tunnel model brackets, and may not cause a similar CFD simulation problem.

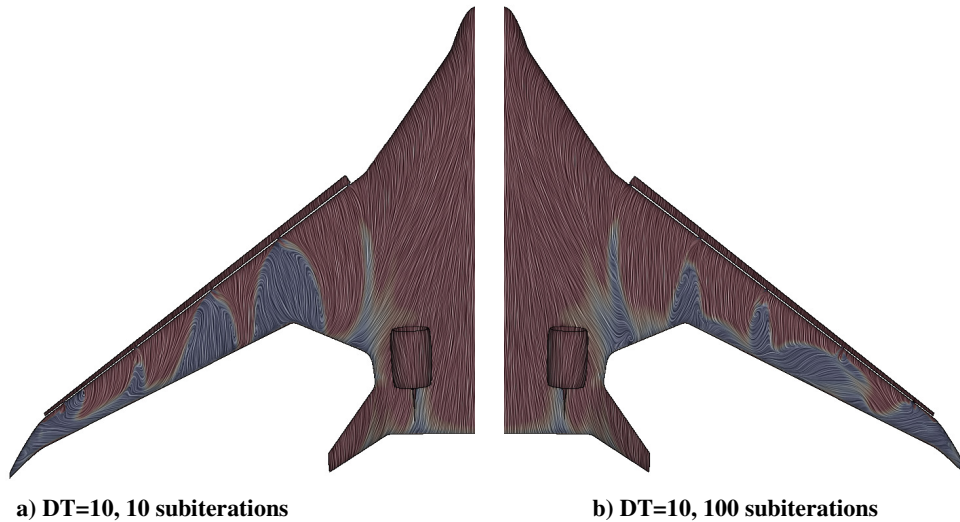


Figure 45. FUN3D Surface flow streamline predictions showing flow separation (reverse flow shown in blue) on upper surface of HWB configuration due to time accuracy convergence at $\alpha=20^\circ$.

V. Conclusions

Computational Fluid Dynamic (CFD) simulations were an integral part of the NASA ERA project. CFD helped support experimentalists in evaluating interference effects due to model support structures, as well as provided alternate support options to reduce unwanted effects for everything from sting selection to aeroacoustic array placement. Multiple CFD solvers, including NASA's OVERFLOW, USM3D, and FUN3D as well as the commercial CFD solver STAR-CCM+, were efficiently and successfully used to provide timely insight into the wind tunnel experimental setup and execution. In addition, through the availability of post-test wind tunnel data, CFD simulation guideline development was possible. A key aspect of this experience was the opportunity to perform this work side-by-side with the wind tunnel experimentalists throughout the project. This made for a well-informed team providing firsthand knowledge on how specific items were being setup in the test as well as how data from the test was to be measured and post-processed for later CFD analysis.

Acknowledgments

The NASA ARMD Environmentally Responsible Aviation Project provided multi-year funding for both the wind tunnel testing and CFD analysis. The authors would like to thank the test teams at NASA Langley's 14x22-foot tunnel, NASA Ames's 40x80-foot tunnel, and the many Boeing support staff who played an integral part in the success of the tests. In addition, the authors would like to thank James C. Ross of NASA Ames Research Center for his assistance in both the acoustic array and acoustic Krueger selection. The NASA Supercomputing System at NASA Ames provided the bulk of the computer resources for this work.

References

- ¹ Collier, F., Thomas, R., Burley, C., Nickol, C., Lee, C. M., Tong, M., "Environmentally Responsible Aviation- Real Solutions for Environmental Challenges Facing Aviation", ICAS 2010-1.6.1, 27th Congress of International Council of the Aeronautical Sciences, September 2010.
- ² Bonet, J. T., Dickey, E., Pricen, N., Sexton, M., Beyar, M., Tompkins, D.M., Kawai, R., Camacho, P., Elmer, K., "Environmentally Responsible Aviation (ERA) Project – Hybrid Wing Body Engine/Airframe Operability Testing Final Report" NASA Contract Report 2015-XXXXXX, 2015.
- ³ CD-adapco website, <http://CD-adapco.com> [retrieved 30 October 2015].
- ⁴ Tramel, R.W., Nichols, R.H., and Buning, P.G., "Addition of Improved Shock-Capturing Schemes to OVERFLOW 2.1," AIAA 2009-3988, Jun. 2009.
- ⁵ Biedron, R. T., Carlson, J., Derlaga, J. M., Gnoffo, P. A., Hammond, D. P., Jones, W. T., Kleb, B., Lee-Rausch, E. M., Nielsen, E. J., Park, M. A., Rumsey, C. L., Thomas, J. L., and Wood, W. A., "FUN3D Manual: 12.7," NASA TM 218761, May 2015.
- ⁶ Chan, W. M., "Developments in Strategies and Software Tools for Overset Structured Grid Generation and Connectivity," AIAA Paper 2011-3051, 20th AIAA Computational Fluid Dynamics Conference, Honolulu, Hawaii, June, 2011.
- ⁷ Suhs, N. E. Rogers, S. E., and Dietz, W. E. "PEGASUS 5: An Automated Pre-processor for Overset-Grid CFD," AIAA Paper 2002-3186, AIAA Fluid Dynamics Conference, June 2002, St. Louis, MO.
- ⁸ Samareh, J., "GridTool: A Surface Modeling and Grid Generation Tool," Proceedings of the Workshop on Surface Modeling, Grid Generation, and Related Issues in CFD Solutions, NASA CP-3291, May 9–11, 1995.
- ⁹ Pirzadeh, S., "Unstructured Viscous Grid Generation by Advancing-Layers Method," AIAA Journal, Vol. 32, No. 8, pp. 1735–1737, August 1994.
- ¹⁰ Pirzadeh, S., "Structured Background Grids for Generation of Unstructured Grids by Advancing Front Method," AIAA Journal, Vol. 31, No. 2, pp. 257–265, February 1993.
- ¹¹ Pointwise, Inc., "Pointwise User Manual, Version 17.3R1", Feb. 2015.
- ¹² Marcum, D. L. and Gaither, J. A., "Mixed Element Type Unstructured Grid Generation for Viscous Flow Applications," 1999, pp. AIAA Paper 1999-3252.
- ¹³ Spalart, P.R. and Allmaras, S.R., "A One-Equation Turbulence Model for Aerodynamic Flows," Recherche Aerospaciale, No. 1, 1994, pp. 5-21.
- ¹⁴ Menter, F. R., "Two-Equation Eddy-Viscosity Turbulence Models for Engineering Applications," AIAA Journal, Vol. 32, No. 8, August 1994, pp. 1598-1605.
- ¹⁵ Langtry, R. B., and Menter, F. R., "Correlation-Based Transition Modeling for Unstructured Parallelized Computational Fluid Dynamics Codes", AIAA Journal, Vol. 47, No. 12, Dec. 2009, pp. 2894-2906.
- ¹⁶ Pulliam, T. H., and Anthony J. S., "High-Lift OVERFLOW Analysis of the DLR-F11 Wind Tunnel Model." 32nd AIAA Applied Aerodynamics Conference. 2014.
- ¹⁷ Shur, M. L., Strelets, M. K., Travin, A. K., Spalart, P. R., "Turbulence Modeling in Rotating and Curved Channels: Assessing the Spalart-Shur Correction," AIAA Journal Vol. 38, No. 5, 2000, pp. 784-792.
- ¹⁸ Spalart, P. R., "Strategies for Turbulence Modelling and Simulation," International Journal of Heat and Fluid Flow, Vol. 21, 2000, pp. 252-263.
- ¹⁹ Mani, M., Babcock, D. A., Winkler, C. M., and Spalart, P. R., "Predictions of a Supersonic Turbulent Flow in a Square Duct," AIAA Paper 2013-0860, January 2013. Turbulence modeling is still the greatest limitation in CFD.
- ²⁰ Pandya, M. J., Abdol-Hamid, K. S., and Frink, N. T., "Enhancement of USM3D Unstructured Flow Solver for High-Speed High-Temperature Shear Flows," AIAA 2009-1329, The 47th AIAA Aerospace Sciences Meeting, January 5-8, 2009.
- ²¹ Frink, N. T., "Tetrahedral Unstructured Navier-Stokes Method for Turbulent Flow," AIAA Journal, Vol. 36, No. 11, Nov. 1998, pp. 1975-1982.
- ²² Hyperwall Reference: <http://www.nasa.gov/centers/ames/multimedia/images/2008/Hyperwall.html>
- ²³ Flamm, J. D., James, K. D., Bonet, J. T., Overview of Low-speed Aerodynamic Tests on a 5.75% Scale Blended-Wing-Body Twin Jet Configuration, AIAA Paper 2016-xxxx, 54th AIAA ASM, 4-8 January 2016, San Diego, CA.
- ²⁴ Herriot, John G.: Blockage Corrections for Three-dimensional-Flow Closed-Throat Wind Tunnels, With Consideration of the Effect of Compressibility, NACA Rep. 995, 1950.
- ²⁵ Quinto, P. Frank; and Orie, Nettie M.: Langley 14- by 22-Foot Subsonic Tunnel Test Engineer's Data Acquisition and Reduction Manual, NASA TM-4563, June 1994.
- ²⁶ Jeffrey, D.R., Zhang, X., Hurst, D.W., "Aerodynamics of Gurney flaps on a single-element high-lift wing", Journal of Aircraft, Vol. 37 No. 2, pp. 295–301, 2000.